Article

Heme Synthesis Inhibition Blocks Angiogenesis via Mitochondrial Dysfunction

Trupti Shetty, Kamakshi Sishtla, Bomina Park, Matthew J. Repass, Timothy W. Corson

tcorson@iu.edu

HIGHLIGHTS

Heme synthesis inhibition changes mitochondrial morphology in endothelial cells

Loss of heme causes buildup of mitochondrial ROS and depolarized membrane potential

Endothelial cells have damaged oxidative phosphorylation and glycolysis on heme loss

Damage is due to loss of heme-containing Complex IV, restored by exogenous heme

iScience

Article

Heme Synthesis Inhibition Blocks Angiogenesis via Mitochondrial Dysfunction

Trupti Shetty,[1,2] Kamakshi Sishtla,[1] Bomina Park,[1,2] Matthew J. Repass,[3,5] and Timothy W. Corson[1,2,4,5,6,*]

SUMMARY

The relationship between heme metabolism and angiogenesis is poorly understood. The final synthesis of heme occurs in mitochondria, where ferrochelatase (FECH) inserts Fe^{2+} into protoporphyrin IX to produce proto-heme IX. We previously showed that FECH inhibition is antiangiogenic in human retinal microvascular endothelial cells (HRECs) and in animal models of ocular neovascularization. In the present study, we sought to understand the mechanism of how FECH and thus heme is involved in endothelial cell function. Mitochondria in endothelial cells had several defects in function after heme inhibition. FECH loss changed the shape and mass of mitochondria and led to significant oxidative stress. Oxidative phosphorylation and mitochondrial Complex IV were decreased in HRECs and in murine retina *ex vivo* after heme depletion. Supplementation with heme partially rescued phenotypes of FECH blockade. These findings provide an unexpected link between mitochondrial heme metabolism and angiogenesis.

INTRODUCTION

An imbalance in mitochondrial metabolism has been implicated in the development of neovascular diseases catalyzed by aberrant angiogenesis. However, the role of heme synthesis in the development of mitochondrial dysfunction in neovascular diseases is unclear.

Neovascularization is a common phenomenon seen in vascular diseases like cancer, type 2 diabetes mellitus, proliferative diabetic retinopathy (PDR), wet age-related macular degeneration (AMD), and retinopathy of prematurity (ROP) (Friedman et al., 2004; Hellstrom et al., 2013; Kempen et al., 2004; Kizhakekuttu et al., 2012). Neovascularization is the disease process where new blood vessels grow from pre-existing ones, and in the eye this can contribute to ocular complications like hemorrhages, retinal detachment, and loss of central vision (Campochiaro, 2013). Endothelial cells (ECs) are key to this process, mediating different cellular functions essential for angiogenesis like proliferation, migration, and vascular permeability (Vandekeere et al., 2015).

We previously reported that heme synthesis inhibition is anti-angiogenic in retinal ECs *in vitro* and in animal models of ocular neovascularization. Blocking heme production in human retinal microvascular ECs (HRECs) decreased proliferation, migration, and endothelial tube formation and caused reduced protein expression of total and phosphorylated VEGF receptor 2 (Basavarajappa et al., 2017). This antiangiogenic effect was only seen in ocular ECs, whereas ocular non-endothelial cells were not similarly affected. Heme synthesis inhibition was associated with smaller ocular neovascular lesions in choroidal and retinal neovascularization mouse models (Basavarajappa et al., 2017; Pran Babu et al., 2020). However, the mechanism underlying this effect remains unknown.

The final synthesis of heme takes place in the mitochondria, when ferrochelatase (FECH) inserts ferrous ion into a precursor protoporphyrin IX (PPIX) to form protoheme (iron-protoporphyrin IX) (Dailey et al., 2017; Nilsson et al., 2009; Poulos, 2014). By directly targeting FECH, cells can be depleted of heme and heme-containing proteins, with a concomitant buildup of PPIX (Atamna et al., 2001; Vijayasarathy et al., 1999). Apart from the role of heme in oxygen transport and storage, heme acts as a prosthetic group in many hemoprotein enzymes involved in oxidative phosphorylation, plus cytochrome P450s, catalases, and nitric oxide synthase (Chiabrando et al., 2014).

[1]Eugene and Marilyn Glick Eye Institute, Department of Ophthalmology, Indiana University School of Medicine, Indianapolis, IN 46202, USA

[2]Department of Pharmacology & Toxicology, Indiana University School of Medicine, Indianapolis, IN 46202, USA

[3]Angio BioCore, Indiana University School of Medicine, Indianapolis, IN 46202, USA

[4]Department of Biochemistry and Molecular Biology, Indiana University School of Medicine, Indianapolis, IN 46202, USA

[5]Melvin and Bren Simon Cancer Center, Indiana University School of Medicine, Indianapolis, IN 46202, USA

[6]Lead Contact

*Correspondence:
tcorson@iu.edu

https://doi.org/10.1016/j.isci.2020.101391

In the present study, we aimed to assess the relationship between mitochondrial physiology in human ECs and heme inhibition. We hypothesized that heme inhibition would lead to defects in heme-containing enzymes of the mitochondrial electron transport chain (ETC) and thus affect mitochondrial function of ECs. We show that loss of heme altered mitochondrial morphology and dynamics, causing increased reactive oxygen species (ROS) levels and depolarized membrane potential. Our studies reveal that heme synthesis is required for EC respiration and complex IV (cytochrome *c* oxidase; CcO) function specifically and can negatively impact glycolytic capacity of ECs. Thus, we characterize a previously unknown role of heme in cellular metabolism that facilitates EC function in angiogenesis.

RESULTS

Heme Inhibition Caused Changes to Mitochondrial Morphology and Increased Oxidative Stress

To block heme production, we used a competitive inhibitor of FECH, the terminal enzyme responsible for catalyzing heme synthesis (Shi and Ferreira, 2006) (see Transparent Methods). Blockade of FECH with active site inhibitor *N*-methylprotoporphyrin (NMPP) causes accumulation of precursor PPIX (Figure S1A). HRECs treated with NMPP showed changes in mitochondrial fragmentation and shape (Figure 1A). NMPP-treated cells had decreased form factor values, indicating reduced mitochondrial branching (Figures 1B and S1B–S1G), owing to more highly fragmented mitochondria (Figure 1A, inset image). Mitochondria appeared less elongated and elliptical in NMPP-treated HRECs as seen by lower aspect ratio values (Figure 1C). To determine mitochondrial mass, we used flow cytometry and quantified median fluorescence intensity (MFI) of NMPP-treated HRECs (Doherty and Perl, 2017). NMPP treatment led to reduced MFI, indicating decreased mass in mitochondria (Figure 1D).

We tested mRNA levels of key mitochondrial fusion proteins involved in mitochondrial dynamics, *MFN2* and *OPA1,* and found significantly lower levels under FECH blockade conditions (Figures 1E and 1F). Fission regulator *DNM1L* (encoding Drp1) showed no change. We measured mitochondrial-specific ROS using MitoSox ROS, and cells treated with NMPP showed a marked increase in ROS levels (Figure 1G). We quantified this increase using flow cytometry and found a significant increase in MitoSox ROS-labeled HRECs treated with NMPP (Figures 1H and 1I). This effect of elevated ROS levels was also seen in RF/6A cells treated with NMPP (Figures S4A and S4B). This primate cell line has properties of chorioretinal ECs (Lou and Hu, 1987) and thus provides corroboration of the primary HREC data.

Loss of FECH Depolarized Mitochondrial Membrane Potential

To assess mitochondrial health, we next measured membrane potential using JC-1, a polychromatic dye that on excitation forms red aggregates and green monomers depending on the energized or deenergized state of mitochondria. Both siRNA-mediated knockdown of FECH and chemical inhibition using NMPP induced loss of healthy red aggregates and an increase in monomers as seen by the green fluorescence (Figures 2A and 2D). This JC-1 excitation was quantified using flow cytometry on HRECs labeled with JC-1 dye and showed reduced red to green fluorescence ratio, indicative of mitochondrial depolarization (Figures 2B, 2C, 2E, and 2F). RF/6A cells also showed depolarized membrane potential after NMPP treatment (Figures S4C–S4E).

Reduced CcO Expression and Activity Rescued by Hemin

To determine where heme depletion was influencing mitochondrial function, we evaluated protein complexes of the ETC after heme inhibition, as complexes II, III, and IV contain heme in their prosthetic groups (Kim et al., 2012). FECH knockdown resulted in a significant decrease of only CcO (Figures 3A and 3B). NMPP-treated cells showed a similar decrease in CcO, and we also found increased expression of Complex V (ATP synthase) upon treatment with this small molecule (Figures 3A and 3C). Additionally, we also assessed mRNA expression of ETC complex genes, *NDUFS1* (complex I), *SDHA* (complex II), *UQCRQ* (complex III), *MT-CO1* (mitochondrially encoded CcO subunit 1), and *COX4I1* (nuclear encoded CcO subunit 1). Only the nuclear-encoded CcO gene showed a significant decrease in mRNA expression (Figure S5A). We then examined the protein levels of heme-containing subunit 1 of CcO (COX4I1) and found a significant decrease under both knockdown and NMPP treatment (Figures 3D–3G). Enzyme activity of CcO was also reduced, and total levels of the complex were significantly reduced after FECH blockade (Figures 3H–3K). Moreover, enzyme activities of complexes I–III remained unaffected (Figures S5B–S5D). To confirm if our results were dependent on heme, we sought to rescue the phenotype of CcO reduction by external
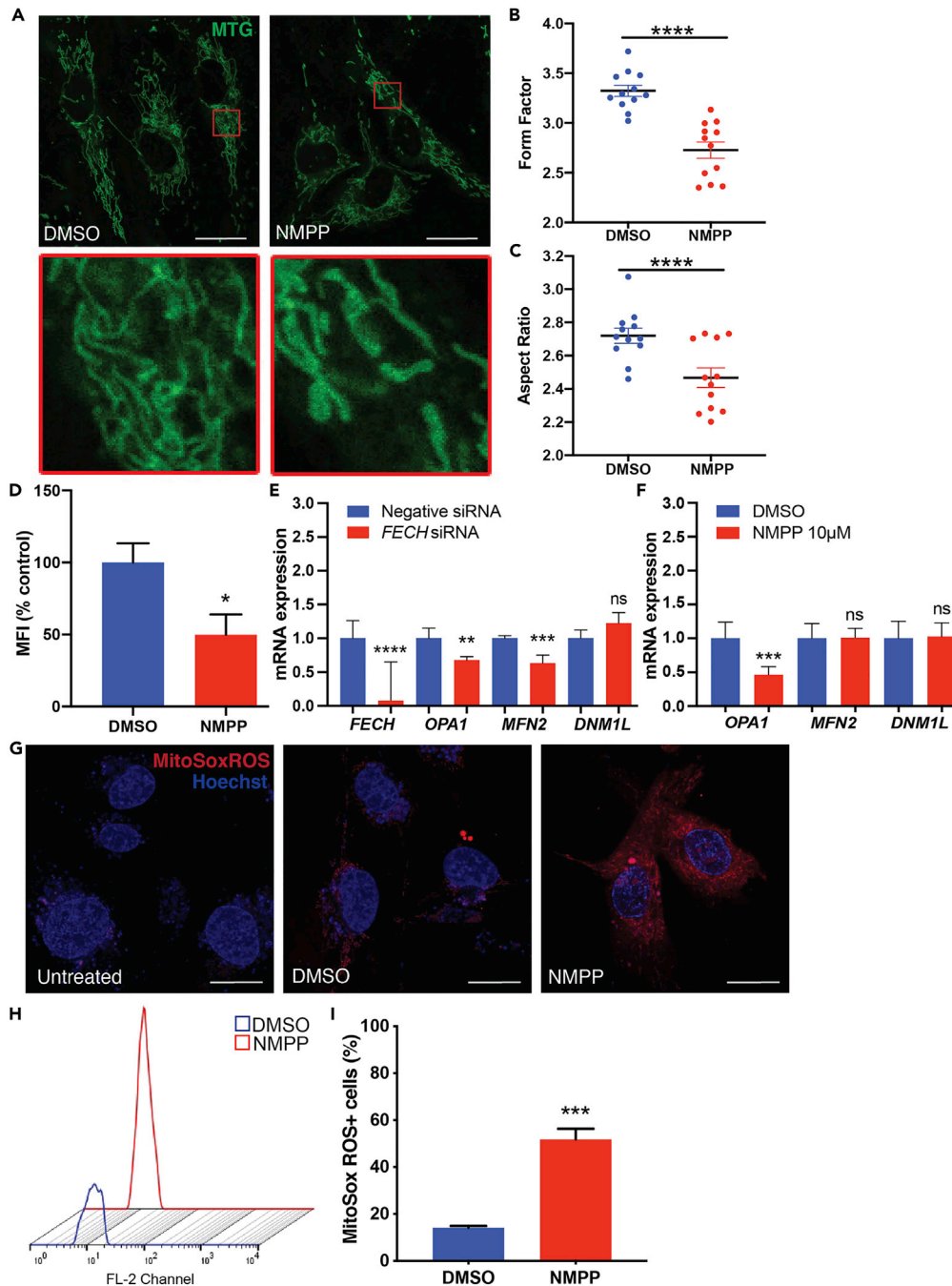
Figure 1. FECH Blockade Altered Mitochondrial Morphology and Increased Oxidative Stress

(A–C) (A) HRECs treated with DMSO or FECH inhibitor NMPP stained with MitoTracker green (MTG). Inset images indicate magnified region marked in red boxes. Form factor (B) and aspect ratio (C) as quantified using ImageJ. Individual data points indicate mean of mitochondria analyzed from each of 12 individual cells per treatment group.

(D–F) (D) Quantification of MTG fluorescence using flow cytometry and calculated median fluorescence intensity (MFI). qPCR analysis of mRNA expression under *FECH* knockdown (E) or NMPP treatment (F).

(G) HRECs stained with mitoSox ROS in red and Hoechst staining in blue.

(H and I) (H) Representative fluorescence peaks as measured by flow cytometry followed by (I) quantification of cells positive for red fluorescence.

Bar graphs indicate mean $\pm$ SEM, n = 3. Representative results from three independent experiments. ns, non-significant, *p < 0.05, **p < 0.01, ***p < 0.001, ****p < 0.0001, two-tailed unpaired Student's t test. Scale bars, 20 μm. See also Figures S1 and S4.
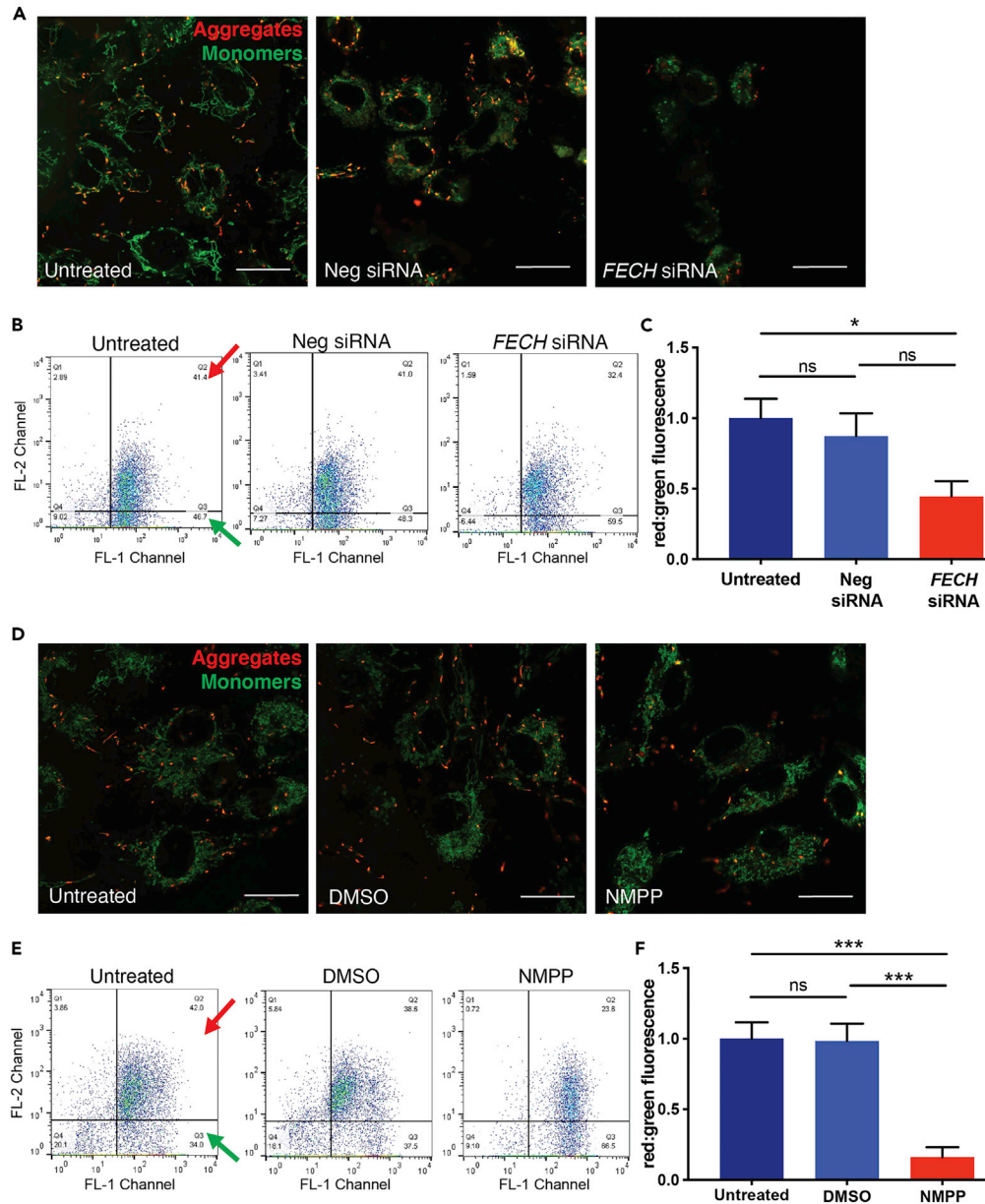
Figure 2. Loss of FECH Reduced Mitochondrial Membrane Potential in HRECs

(A–F) HRECs stained with JC-1 dye showing green monomers and red aggregates under *FECH* knockdown condition (A) and NMPP treatment (D). Representative dot plots of FL1 versus FL2 channel from three individual experiments, measuring red and green fluorescence using flow cytometry after *FECH* knockdown (B) and NMPP treatment (E). Red and green arrows indicate quadrants expressing FL1-red and FL2-green fluorescent cells. (C and F) Quantification of red:green fluorescence from flow experiment. Bar graphs indicate mean $\pm$ SEM, n = 3; ns, non-significant, *p < 0.05, ***p < 0.001, one-way ANOVA with Tukey's post hoc tests. Scale bars, 20 μm. See also Figure S4.

supplementation of heme to the cells. Hemin, a stable form of heme, was able to alleviate CcO protein expression depletion and partially rescue CcO enzyme activity (Figures 3L–3N). RF/6A cells showed a similar rescue phenotype of CcO enzyme after heme addition (Figures S6A–S6D). We also used another heme synthesis inhibitor, succinylacetone, which blocks the second committed enzyme in heme synthesis, 5-aminolevulinic acid dehydratase (ALAD), upstream of the PPIX-FECH step (Dailey et al., 2017; Vande-keere et al., 2018). HRECs treated with succinylacetone showed reduction in protein expression of CcO and also Complex III (Figures S7A and S7B).
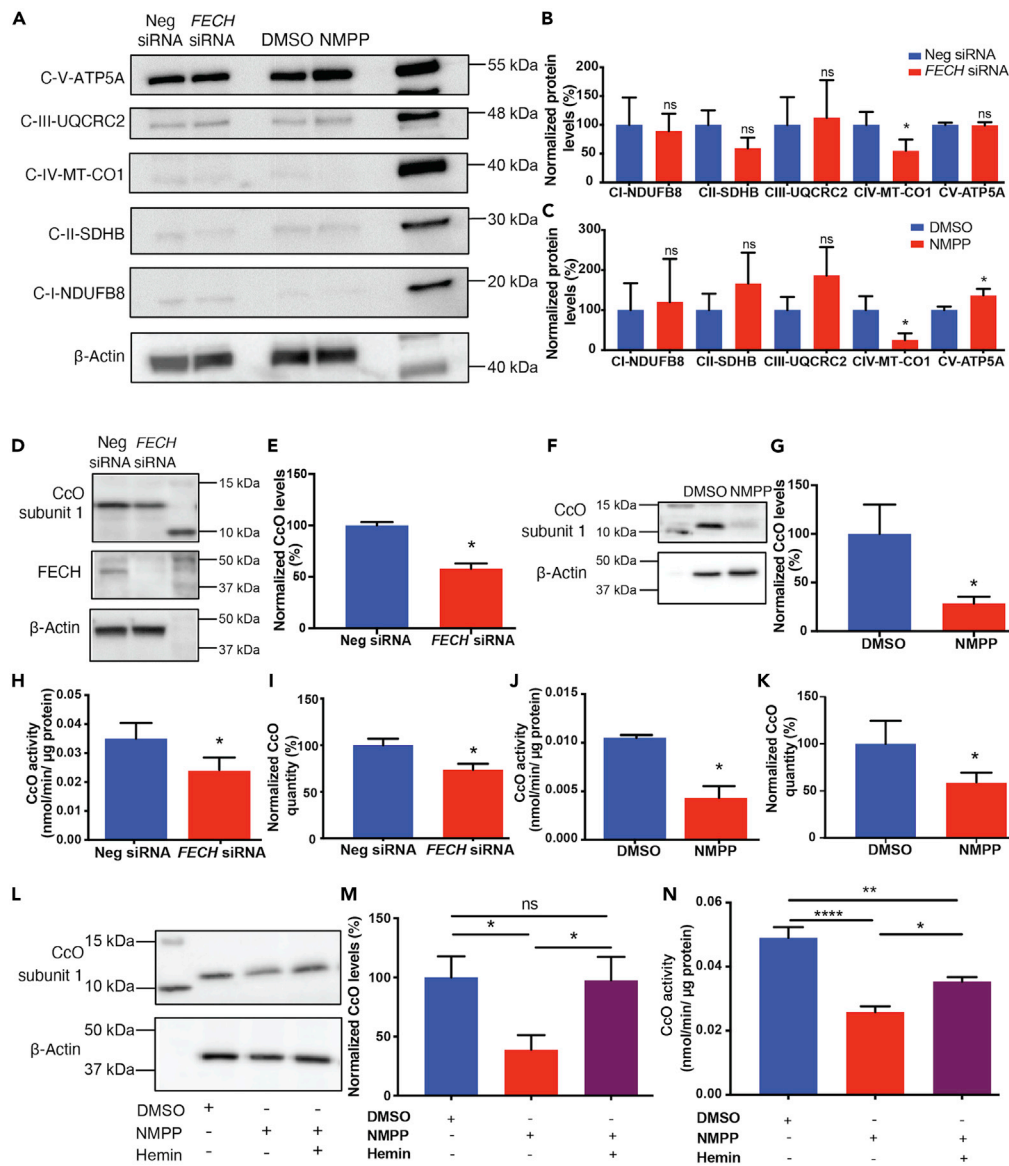
Figure 3. FECH Inhibition Caused Reduced CcO Expression, Rescued by Hemin

(A) HRECs under *FECH* siRNA or NMPP-treated conditions were immunoblotted for Complexes I–V as indicated.

(B and C) Quantification of the blots was graphed as shown relative to appropriate control.

(D) *FECH* siRNA-treated HRECs were probed for CcO nuclear encoded subunit 1 (COX4I1) and FECH along with housekeeping control and (E) quantified. Similarly, HRECs treated with NMPP were blotted for CcO subunit 1 (F) with (G) quantification as shown. CcO enzyme activity was measured under *FECH* knockdown condition (H) and NMPP treatment (J) and total CcO levels were quantified by ELISA for both the conditions (I and K).

(L and M) CcO protein expression and quantification under defined conditions.

(N) CcO enzyme activity was partially rescued in NMPP-treated cells exposed to hemin. Immunoblot images representative from three independent experiments.

Bar graphs indicate mean ± SEM, n = 3–4; ns, non-significant, *p < 0.05, **p < 0.01, ****p < 0.0001. (B, C, E, G, H–K) unpaired Student's t test (M and N) one-way ANOVA with Tukey's post hoc tests. See also Figures S5–S7.

FECH Blockade Reduced Mitochondrial Function of Retinal ECs

To understand whether loss of function of an important complex in the ETC resulted in defects in mitochondrial respiration, we assessed maximal oxygen consumption rate (OCR) induced by the potential gradient uncoupler FCCP (Figures S2A and S2B). FCCP induces uninhibited flow of electrons across the ETC, causing the enzymes of the respiratory chain to use metabolic substrates at full potential and, in turn,

revealing the maximal cellular capacity that can meet energy demands under metabolically stressed conditions (Dranka et al., 2011). Under metabolic stress, both HRECs and RF/6A cells underwent increased glycolysis to meet energy demands (Figures S2C–S2F).

Based on these optimized parameters (Figure S3), we measured OCR of HRECs after FECH knockdown and observed reduced basal respiration (Figures 4A and 4B). Uncoupler-induced maximal respiration was significantly decreased, with a marked reduction also found in OCR-linked ATP production and spare respiratory capacity (Figures 4C–4E). Similarly, NMPP treated cells showed a dose-dependent decrease in basal (Figures 4F and 4G) and maximal respiration (Figure 4H) along with a decline in OCR-linked ATP production and spare respiratory capacity (Figures 4I and 4J). We saw a similar decrease in mitochondrial respiratory activity in RF/6A cells (Figures S6E–S6I). Succinylacetone-treated HRECs also showed a decrease in basal and maximal respiration along with reduced OCR-linked ATP production and spare respiratory capacity (Figures S7C–S7G).

Inhibition of FECH Led to Decreased Glycolytic Function

Microvascular ECs are highly glycolytic compared with other cell types (De Bock et al., 2013). Under mitochondrial stress, both HREC and RF/6A cells had increased glycolysis over mitochondrial respiration in our system (Figures S2C–SF). Hence, we next investigated this key cellular energetic pathway in HRECs by measuring changes in the pH of the extracellular medium. Cells were briefly starved in glucose-deficient medium, followed by induction of glycolysis using a saturating dose of glucose. Interestingly, HRECs under siRNA-mediated FECH knockdown and NMPP treatment each had decreased glycolytic capacity and glycolysis (Figures 5A–5C and 5E–5G). Both conditions depleted glycolytic reserve, as seen by a marked decrease in ECAR after 2-DG injection (Figures 5D and 5H).

FECH Inhibition *In Vivo* Caused Impaired Mitochondrial Energetics in Retina

We further determined if the effect of NMPP had the same phenotype *in vivo* in an intact eye. For this, we administered NMPP intravitreally to mice and measured OCR of retina in an *ex vivo* assay (Figure 6A). We found that retinas treated with NMPP had a significant decrease in basal respiration and a similar decline in maximal respiration (Figures 6B and 6C). Spare respiratory capacity was severely reduced in the retinas of NMPP-treated animals compared with their vehicle-treated counterparts (Figure 6D). We also observed about a 30% reduction in protein expression of subunit 1 of CcO in the NMPP-treated retinas (Figures 6E and 6F).

DISCUSSION

Heme synthesis blockade suppresses pathological angiogenesis by poorly understood mechanisms. In the present study, we sought to investigate the effects of heme inhibition on the mitochondrial function of retinal ECs by directly studying heme-containing complexes of the ETC and documenting mitochondrial physiology under heme depletion.

The mitochondrial ETC is a major source of ROS induced by vascular endothelial growth factor (VEGF) in hyperglycemic and hypoxic cellular environments (Cheng et al., 2011; Pearlstein et al., 2002; Wang et al., 2018). In PDR, increased mitochondrial ROS and impaired Ca^{2+} signaling can cause an increase in oxidative stress (Kowluru and Mishra, 2015; Pangare and Makino, 2012; Tang et al., 2014; Wang et al., 2018). Complex III of the ETC was recently shown to be important for umbilical vein EC respiration and thus proliferation during angiogenesis (Diebold et al., 2019). Mitochondrial dysfunction in the retinal pigment epithelium and photoreceptors has been reported for wet AMD (Barot et al., 2011; Lefevere et al., 2017), but evidence in retinal ECs is limited. Metabolic factors like succinate and adenosine, generated from the Krebs cycle and ATP metabolism, respectively, are proangiogenic for hypoxia-driven neovascularization (Sapieha et al., 2010). However, the exact mechanism of how metabolites disrupt mitochondrial energetics in ischemic retinal ECs remains unclear (Grant et al., 1999; Sapieha et al., 2008).

Mitochondrial dysfunction in ECs leads to pathological angiogenesis. Heme and heme-containing enzymes play a significant role in this process, but the linkage between these phenomena has not been extensively explored. Serine synthesis deficiency induced heme depletion in ECs and caused decreased mitochondrial respiration and multiorgan angiogenic defects in animals (Vandekeere et al., 2018), whereas heme accumulation in ECs due to an altered heme exporter affects angiogenesis and causes endoplasmic reticulum stress (Petrillo
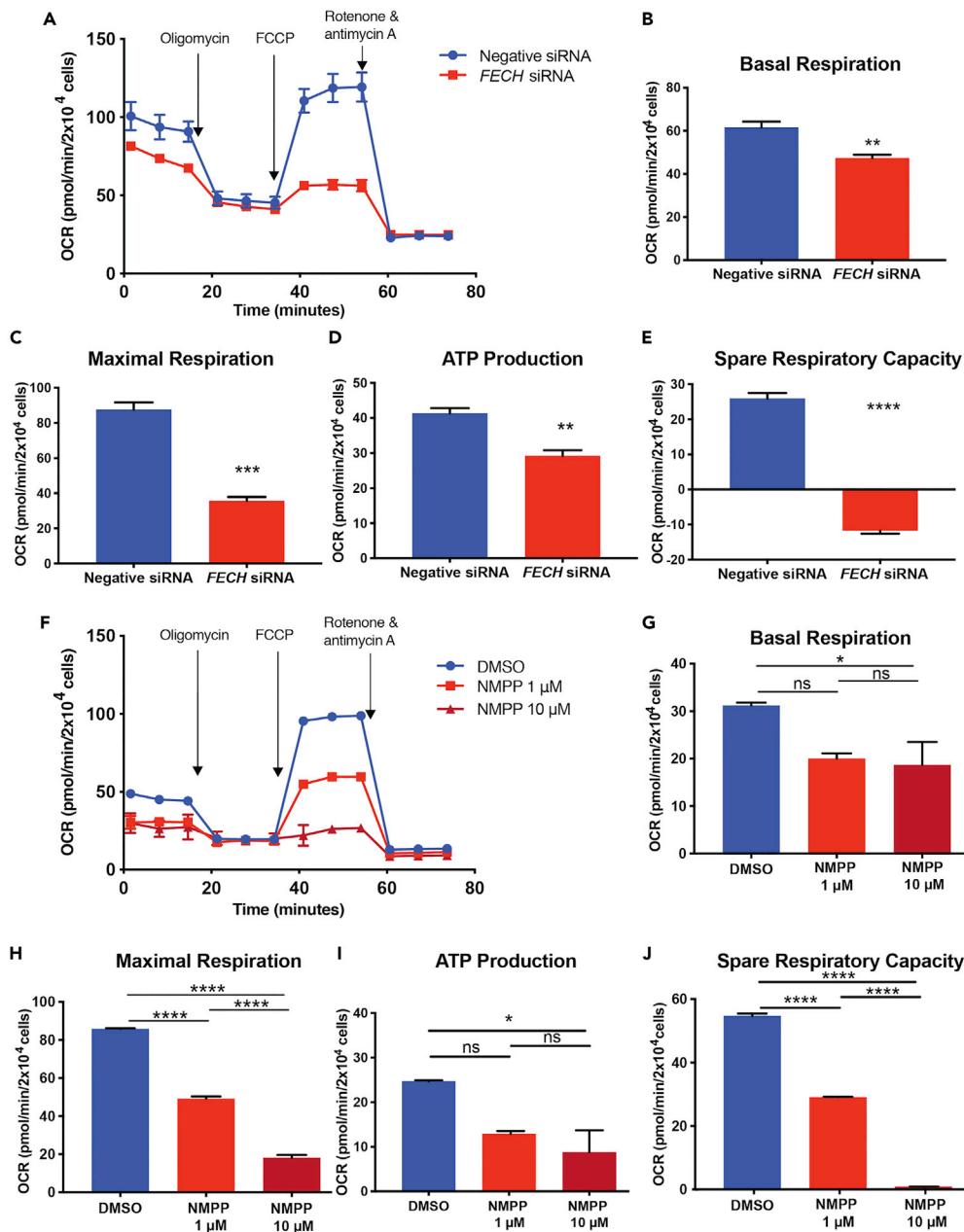
Figure 4. Loss of FECH Reduced Mitochondrial Respiration

(A and F) OCR kinetic traces for HRECs under *FECH* knockdown or NMPP chemical inhibition.

(B and G) Basal respiration.

(C and H) Maximal respiration.

(D and I) OCR-linked ATP production, and (E and J) spare respiratory capacity were calculated based on OCR curves for the respective treatment group.

(A and F) Representative OCR curve of three individual experiments. Bar graphs indicate mean ± SEM, n = 3; *p < 0.05, **p < 0.01, ***p < 0.001, ****p < 0.0001 (B, C, D, and E) unpaired Student's t test (G, H, I, and J) one-way ANOVA with Tukey's post hoc tests. See also Figures S6 and S7.

et al., 2018). Apart from ECs, non-small cell lung carcinoma cells with elevated heme synthesis levels had increases in enzyme activities of the ETC. Increased production of heme was associated with increased migratory and invasive properties of these cells and xenograft tumors in mice (Sohoni et al., 2019). Here, we demonstrated how heme depletion by blockade of the terminal synthesis enzyme FECH led to defects in CcO and ETC
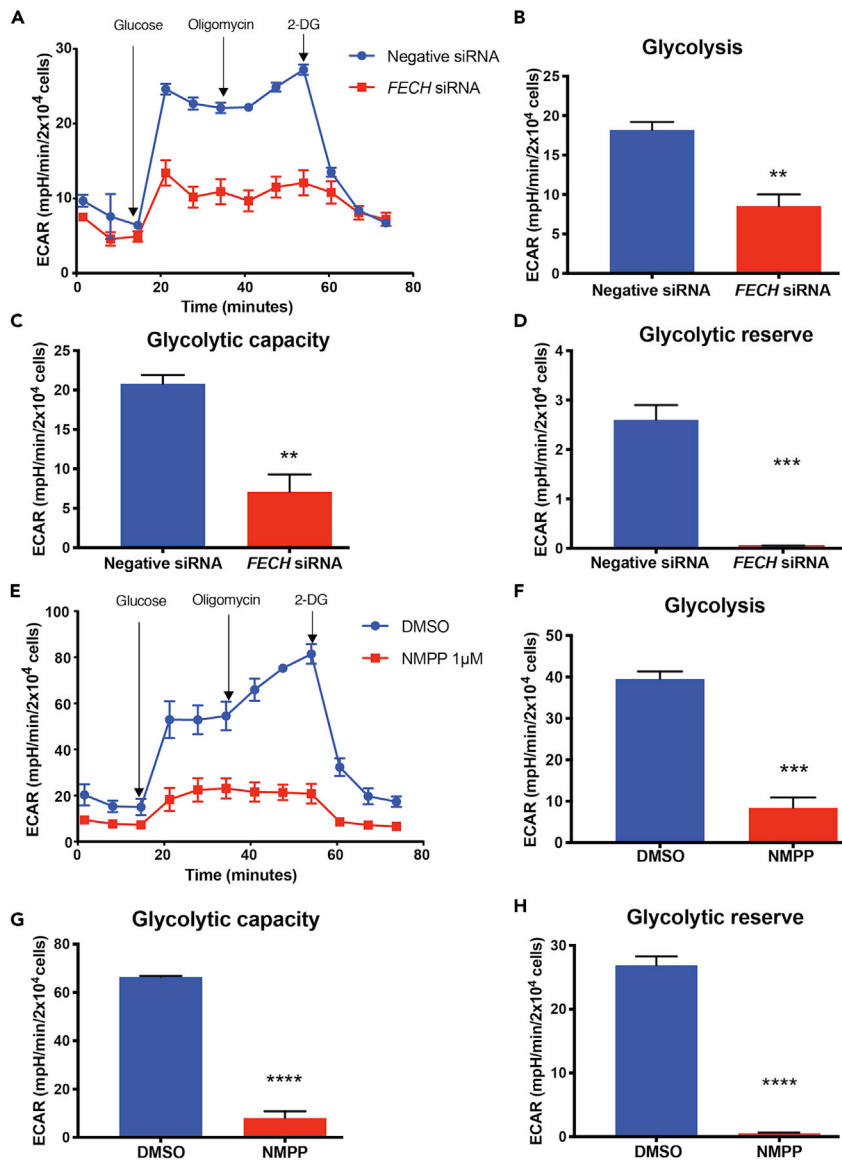
Figure 5. FECH Inhibition Caused a Decrease in Glycolytic Function

(A–H) (A and E) ECAR kinetic traces for HRECs under *FECH* knockdown or NMPP chemical inhibition. (B and F) Glycolysis, (C and G) glycolytic capacity, and (D and H) glycolytic reserve were calculated based on ECAR curves for the respective treatment group.

(A and E) Representative ECAR curve of three individual experiments. Bar graphs indicate mean $\pm$ SEM, n = 3; **p < 0.01, ***p < 0.001, ****p < 0.0001, unpaired Student's t test. 2-DG, 2-deoxyglucose.

disruption (Figure 7). Retinal and choroidal ECs alike have increased mitochondrial-specific oxidative stress, dysfunctional mitochondrial physiology, and disruption of glycolysis as a result of these defects.

Changes to mitochondrial morphology can indicate alterations in mitochondrial dynamics and cellular function. Our findings of reduced form factor and aspect ratio after FECH blockade indicate greater fragmentation and decreased length (Duraisamy et al., 2019; Picard et al., 2013). Furthermore, reduced mitochondrial mass was evident by our flow cytometric analysis. HRECs after heme depletion also had reduced *MFN2* and *OPA1* transcript levels. Reduction of these mitochondrial fusion protein marker genes confirms a change in mitochondrial dynamics. An increase in fragmented mitochondria also leads to increased ROS levels (Jezek et al., 2018), as confirmed by our results. Moreover, disruption of fusion proteins can also lead to an increase in ROS levels
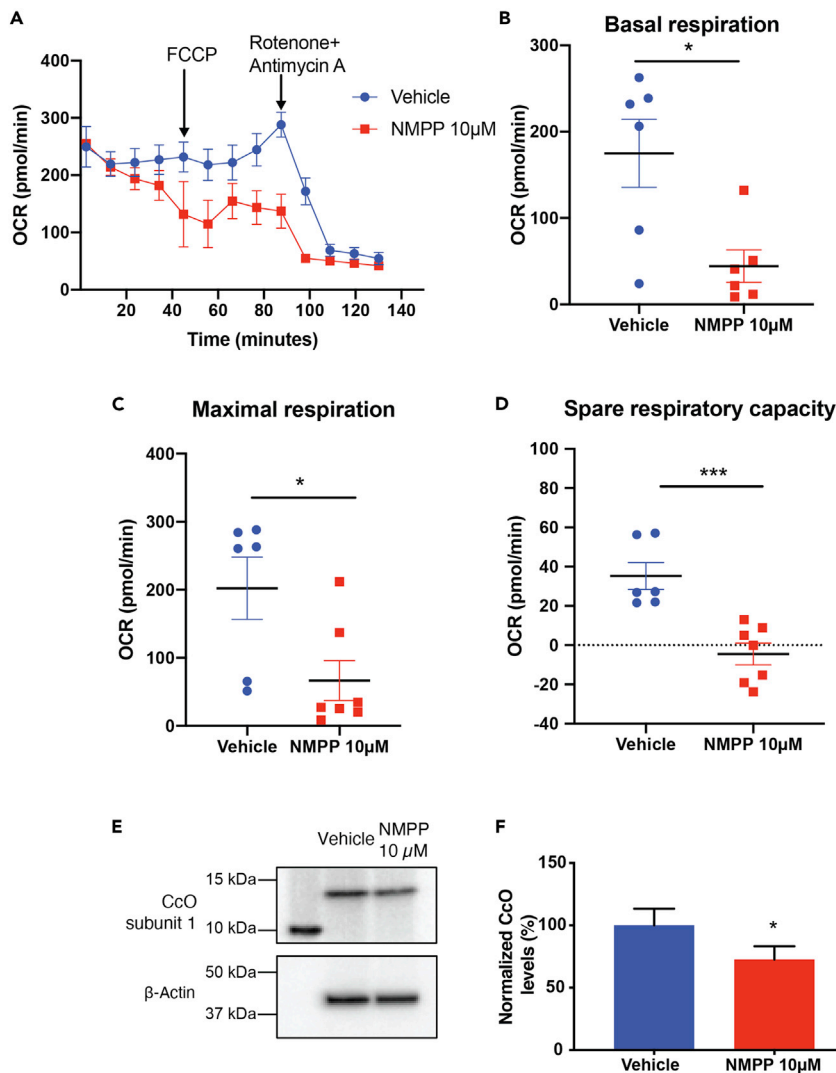
Figure 6. FECH Inhibition *In Vivo* Decreased Mitochondrial Respiration in Retina

(A) Representative OCR kinetic traces for retina from animals treated with NMPP.

(B–D) (B) Basal respiration, (C) maximal respiration, and (D) spare respiratory capacity were calculated based on OCR curves for the respective treatment groups.

(E) Immunoblot showing CcO nuclear encoded subunit 1 (COX4I1) protein expression from three pooled retinal tissue lysates from NMPP treated eyes and (F) quantification of immunoblots. Graphs indicate mean ± SEM for two tissue punches from each retina per treatment group, n = 6–7 per treatment condition. *p < 0.05, ***p < 0.001, unpaired Student's t test.

(Kim et al., 2018), as also evident in our cell model. Although we did not observe any change in fission protein expression, decreased *MFN2* is also consistent with the smaller, fragmented mitochondria we observed, similar to those seen in diabetic mouse coronary ECs (Makino et al., 2010).

Inner mitochondrial membrane potential ($\Delta\Psi_m$) was considerably decreased after FECH knockdown or NMPP treatment. This finding was explained by our result of reduced CcO expression and activity, which might have collapsed the potential gradient and caused a reduced membrane potential. Our mitochondrial energetics findings further support this result. A significant reduction in FCCP-induced maximal respiration indicates defective CcO, which is unable to perform the role of electron transfer. Uncoupling brought on by FCCP causes the ETC to rely on CcO to carry out oxidative phosphorylation by the free-flowing electrons (Dranka et al., 2011). Under FECH inhibition conditions, FCCP-induced maximal respiration was affected, indicating CcO dysfunction due to heme loss.
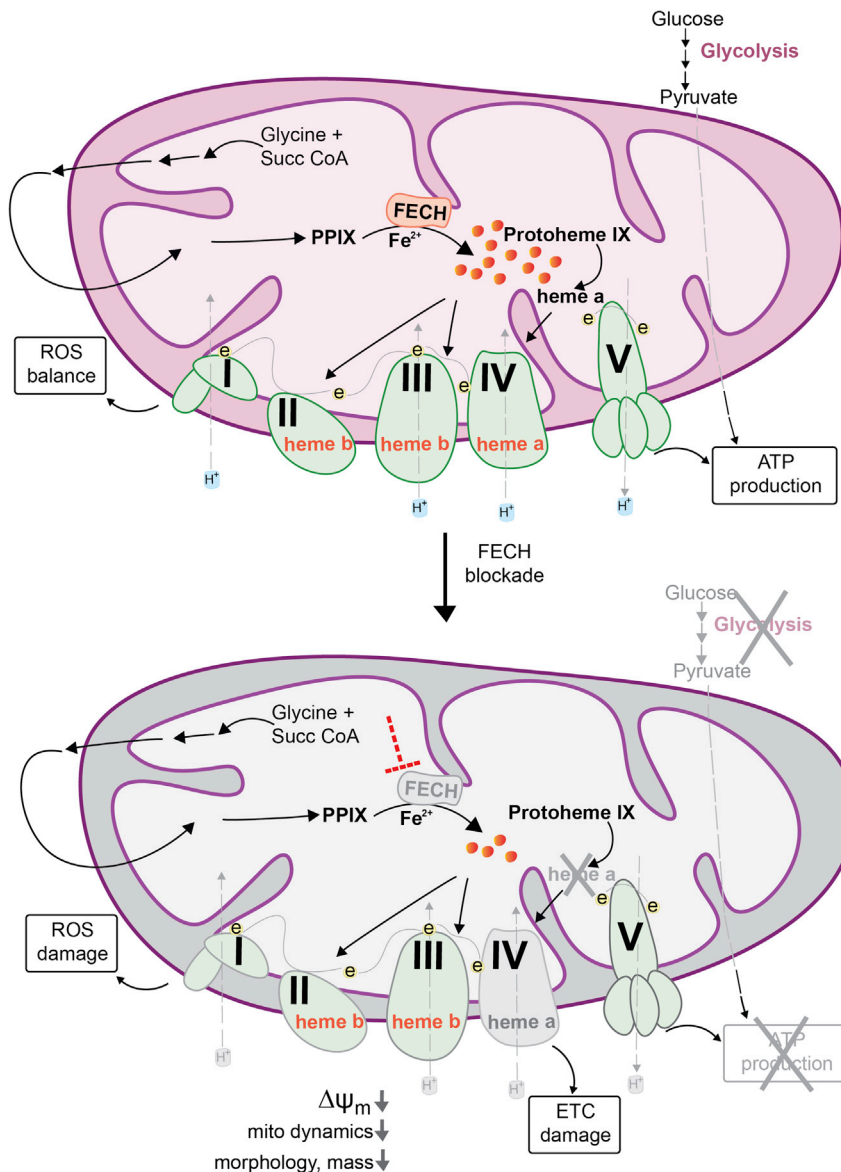
Figure 7. Schematic Model of Mitochondrial Dysfunction on Heme Loss

Heme synthesis begins with the condensation of glycine and succinyl CoA in the mitochondrial matrix. The final step is the insertion of ferrous ion into protoporphyrin IX (PPIX), catalyzed by ferrochelatase (FECH) to produce protoheme (also known as heme b). Protoheme and its derivatives are available for different cellular enzymes, including complexes of the ETC (e, electrons). Heme *a* is synthesized by sub-hemylation steps and utilized by CcO (Complex IV) for composition of the holoenzyme. Heme synthesis blockade by inhibiting the terminal synthesis enzyme FECH leads to CcO defects and disrupts cellular energetics. Mitochondrial dynamics is altered with reduced fusion and mass, depolarized membrane potential ($\Delta\Psi_m$) and elevated reactive oxygen species (ROS).

Heme depletion by directly blocking FECH primarily affected levels and activity of CcO of all the other heme-containing complexes of the ETC in ECs of the retina and choroid. CcO subunit 1 contains heme *a* and a_3 (not found in complexes I–III and V). Heme *a* is made in a series of sub-synthesis hemylation steps carried out by heme *a* synthase and is essential for proper folding and stability of CcO (Kim et al., 2012) (Figure 7). CcO is particularly sensitive to FECH inhibition-induced heme depletion, possibly affecting the hemylation process downstream of protoheme synthesis, leading to a smaller pool of heme *a* (Atamna et al., 2001; Sinkler et al., 2017). COX10 and COX15, proteins responsible for conversion of heme *b* (synthesized by FECH) to heme *a* were among the top-scoring genes that caused ETC disruption after heme

depletion in acute myeloid leukemia cells (Lin et al., 2019), further suggesting the significance of heme a supply as a mediator of mitochondrial function, since it is a prosthetic group specifically in CcO holoenzyme. Furthermore, blocking the skeletal muscle-specific subunit 7a of CcO decreased mitochondrial ATP production in mouse hindlimb muscles. Interestingly, this was associated with reduced muscle angiogenesis and decreased capillarity (Lee et al., 2012), further supporting a link between CcO and EC function. Our findings on the mRNA and protein levels plus enzyme activities of all ETC complexes are consistent with this hypothesis that FECH inhibition preferentially disrupts CcO expression and function.

Loss of functional CcO was restored at least partially by extracellular heme supplementation. Additionally, blocking heme synthesis upstream of FECH by using succinylacetone also led to a similar mitochondrial phenotype as FECH blockade. This suggests that the EC phenotype after FECH inhibition is heme dependent and not due to an off-target effect of NMPP or due to PPIX buildup/toxicity (Wyld et al., 1997). NMPP caused significant overexpression of complex V (not seen under FECH knockdown), which could be a secondary effect of damage to CcO, causing compensatory upregulation of ATP synthase (Havlickova Karbanova et al., 2012; Rolland et al., 2013). Notably, succinylacetone produced a decrease in both Complex III and CcO, perhaps due to a more profound heme synthesis blockade than that achieved by FECH inhibition or knockdown. Our studies previously reported effects of NMPP and FECH knockdown specific to ECs of retina, choroid, brain, and umbilical vein, and we did not observe a similar anti-proliferative phenotype on FECH blockade in other ocular cell types of non-endothelial origin (Basavarajappa et al., 2017). However, the phenotype of FECH deficiency on ETC complexes in other cell types beyond ECs would be an interesting aspect for future exploration.

Perhaps non-endothelial cell types can meet their energy demands from the glycolysis pathway in the event of heme depletion-induced ETC dysfunction (Rafikov et al., 2015). Conversely, loss of mitochondrial respiration in ECs due to lack of functional oxidative phosphorylation did not result in compensation by the glycolysis pathway in ECs (Zielinski et al., 2016). ECs rely upon aerobic glycolysis for nearly 85% of their energy, a feature that is highly active during aberrant angiogenesis (De Bock et al., 2013). Severe heme depletion could possibly disrupt $NADH/H^+$ and redox homeostasis, as already evident from ETC dysfunction. Moreover, increased ROS levels in ECs can shift their metabolic needs to accommodate cellular damage and dysfunction, in which case both cellular energetic systems are collapsed (Vandekeere et al., 2018; Warren et al., 2014; Wellen and Thompson, 2010). Interestingly, mitochondrial transcription of CcO subunit 1 (*MT-CO1*) mRNA is not affected after heme loss (although protein levels were decreased), but the nuclear encoded CcO gene *COX4I1* was significantly decreased at both the mRNA and protein levels after FECH inhibition. This is in keeping with heme acting at the post-transcriptional level to stabilize the assembly of the CcO subunits with minimal effect on CcO mitochondrial transcription itself.

In summary, our findings provide a previously unidentified link between heme synthesis, angiogenesis, and mitochondrial energetics. Specifically, heme synthesis blockade via FECH leads to a reduction in heme availability for hemoprotein components of the ETC, notably CcO, likely due to a shortage of heme a and a_3. This is then associated with reduced oxidative phosphorylation, with concomitant loss of mitochondrial membrane potential and changes in mitochondrial shape and dynamics, as well as increased ROS production (Figure 7). Blockade of heme during the early stages of the pathway (via ALAD) disrupts heme b synthesis, affecting the ETC proteins beyond just Complex IV. This potentially explains how ECs rely on a constant supply of heme during increased energy demands, essential for the formation of neovessels. The role of heme synthesis in mitochondrial function and pathological angiogenesis has been overlooked. Our observations bridge this gap in knowledge by characterizing the metabolic phenotype of ECs under heme deficiency. Loss of heme provokes prominent anti-angiogenic effects that might be exploited therapeutically for neovascular eye disease. Our findings invite future studies to further our understanding of metabolic dysfunction in neovascularization.

Limitations of the Study

Retinal ECs are technically laborious for experimental manipulations. Apart from being difficult to transfect, low absolute heme levels precluded spectral determination of hemes a, b, and c. NMPP as a FECH inhibitor could be deleterious to other hemoproteins in ECs and could have off-target effects, although we titrated NMPP to well below toxic levels in these studies and complemented NMPP findings with a knockdown approach and succinylacetone treatment. Similarly, using hemin to rescue FECH inhibition-induced heme depletion has limitations. Hemin itself can introduce mitochondrial toxicity (Higdon et al., 2012), and complete rescue of ETC damage through hemin supplementation is challenging. Additionally, damage to CcO due to insufficient heme could impair formation of ETC supercomplexes (Acin-Perez et al.,

2008), which was not assessed in our study. Resolving mitochondrial lysates isolated from NMPP-treated ECs in their endogenous form, for example, by a native gel electrophoresis method, could identify disruption to the assembly of these complexes (Jha et al., 2016).

We previously tested a genetic mouse model with a M98K point mutation in the *Fech* gene (*Fech*[m1Pas]) leading to deficiency in FECH activity and found reduced neovascular lesions in the eye (Basavarajappa et al., 2017; Pran Babu et al., 2020). This *Fech*[m1Pas] mouse model shows pronounced PPIX buildup and *increased* mitochondrial respiratory activity, specifically CcO (Navarro et al., 2005), likely a compensatory response to constitutive heme depletion. This renders them problematic for corroborating our findings *in vivo*. Moreover, complete loss of function of FECH is incompatible with survival (Magness et al., 2002). For these reasons, for *in vivo* validation we employed here an acute model of FECH blockade using local administration of NMPP intravitreally. Nonetheless, this FECH inhibition *in vivo* had energetic effects in the retina similar to those seen on retinal and choroidal ECs cultured *in vitro*. However, an important limitation is that this technique cannot distinguish the energetic profiles of ECs from other cell types present in the retina.

Resource Availability

Lead Contact

Further information and requests for resources and reagents should be directed to and will be fulfilled by the Lead Contact, Timothy W. Corson (tcorson@iu.edu).

Materials Availability

This study did not generate new unique reagents.

Data and Code Availability

The published article includes all datasets generated or analyzed during this study.

METHODS

All methods can be found in the accompanying Transparent Methods supplemental file.

SUPPLEMENTAL INFORMATION

Supplemental Information can be found online at https://doi.org/10.1016/j.isci.2020.101391.

AUTHOR CONTRIBUTIONS

Conceptualization, T.S. and T.W.C.; Investigation, T.S., K.S., B.P., and M.J.R.; Formal Analysis and Visualization, T.S.; Writing – Original Draft, T.S.; Writing – Review & Editing, T.S., K.S., B.P., M.J.R., and T.W.C.; Funding Acquisition, T.W.C.

DECLARATION OF INTERESTS

T.W.C. is a named inventor on patent applications related to this work. The other authors declare no competing interests.

REFERENCES

Acin-Perez, R., Fernandez-Silva, P., Peleato, M.L., Perez-Martos, A., and Enriquez, J.A. (2008). Respiratory active mitochondrial supercomplexes. Mol. Cell 32, 529–539.

Atamna, H., Liu, J., and Ames, B.N. (2001). Heme deficiency selectively interrupts assembly of mitochondrial complex IV in human fibroblasts: revelance to aging. J. Biol. Chem. 276, 48410–48416.

Barot, M., Gokulgandhi, M.R., and Mitra, A.K. (2011). Mitochondrial dysfunction in retinal diseases. Curr. Eye Res. 36, 1069–1077.

Basavarajappa, H.D., Sulaiman, R.S., Qi, X., Shetty, T., Sheik Pran Babu, S., Sishtla, K.L., Lee, B., Quigley, J., Alkhairy, S., Briggs, C.M., et al. (2017). Ferrochelatase is a therapeutic target for ocular neovascularization. EMBO Mol. Med. 9, 786–801.

De Bock, K., Georgiadou, M., Schoors, S., Kuchnio, A., Wong, B.W., Cantelmo, A.R., Quaegebeur, A., Ghesquiere, B., Cauwenberghs, S., Eelen, G., et al. (2013). Role of PFKFB3-driven glycolysis in vessel sprouting. Cell 154, 651–663.

Campochiaro, P.A. (2013). Ocular neovascularization. J. Mol. Med. (Berl) 91, 311–321.

Cheng, X., Siow, R.C., and Mann, G.E. (2011). Impaired redox signaling and antioxidant gene expression in endothelial cells in diabetes: a role for mitochondria and the nuclear factor-E2-related factor 2-Kelch-like ECH-associated protein 1 defense pathway. Antioxid. Redox Signal. 14, 469–487.

Chiabrando, D., Vinchi, F., Fiorito, V., Mercurio, S., and Tolosano, E. (2014). Heme in pathophysiology: a matter of scavenging, metabolism and trafficking across cell membranes. Front. Pharmacol. 5, 61.

Dailey, H.A., Dailey, T.A., Gerdes, S., Jahn, D., Jahn, M., O'Brian, M.R., and Warren, M.J. (2017). Prokaryotic heme biosynthesis: multiple pathways to a common essential product. Microbiol. Mol. Biol. Rev. 81, e00048–16.

Diebold, L.P., Gil, H.J., Gao, P., Martinez, C.A., Weinberg, S.E., and Chandel, N.S. (2019). Mitochondrial complex III is necessary for endothelial cell proliferation during angiogenesis. Nat. Metab. 1, 158–171.

Doherty, E., and Perl, A. (2017). Measurement of mitochondrial mass by flow cytometry during oxidative stress. React. Oxyg Species (Apex) 4, 275–283.

Dranka, B.P., Benavides, G.A., Diers, A.R., Giordano, S., Zelickson, B.R., Reily, C., Zou, L., Chatham, J.C., Hill, B.G., Zhang, J., et al. (2011). Assessing bioenergetic function in response to oxidative stress by metabolic profiling. Free Radic. Biol. Med. 51, 1621–1635.

Duraisamy, A.J., Mohammad, G., and Kowluru, R.A. (2019). Mitochondrial fusion and maintenance of mitochondrial homeostasis in diabetic retinopathy. Biochim. Biophys. Acta Mol. Basis Dis. 1865, 1617–1626.

Friedman, D.S., O'Colmain, B.J., Munoz, B., Tomany, S.C., McCarty, C., de Jong, P.T., Nemesure, B., Mitchell, P., and Kempen, J.; Eye Diseases Prevalence Research Group (2004). Prevalence of age-related macular degeneration in the United States. Arch. Ophthalmol. 122, 564–572.

Grant, M.B., Tarnuzzer, R.W., Caballero, S., Ozeck, M.J., Davis, M.I., Spoerri, P.E., Feoktistov, I., Biaggioni, I., Shryock, J.C., and Belardinelli, L. (1999). Adenosine receptor activation induces vascular endothelial growth factor in human retinal endothelial cells. Circ. Res. 85, 699–706.

Havlickova Karbanova, V., Cizkova Vrbacka, A., Hejzlarova, K., Nuskova, H., Stranecky, V., Potocka, A., Kmoch, S., and Houstek, J. (2012). Compensatory upregulation of respiratory chain complexes III and IV in isolated deficiency of ATP synthase due to TMEM70 mutation. Biochim. Biophys. Acta 1817, 1037–1043.

Hellstrom, A., Smith, L.E., and Dammann, O. (2013). Retinopathy of prematurity. Lancet 382, 1445–1457.

Higdon, A.N., Benavides, G.A., Chacko, B.K., Ouyang, X., Johnson, M.S., Landar, A., Zhang, J., and Darley-Usmar, V.M. (2012). Hemin causes mitochondrial dysfunction in endothelial cells through promoting lipid peroxidation: the protective role of autophagy. Am. J. Physiol. Heart Circ. Physiol. 302, H1394–H1409.

Jezek, J., Cooper, K.F., and Strich, R. (2018). Reactive oxygen species and mitochondrial dynamics: the yin and yang of mitochondrial dysfunction and cancer progression. Antioxidants (Basel) 7, 13.

Jha, P., Wang, X., and Auwerx, J. (2016). Analysis of mitochondrial respiratory chain supercomplexes using blue native polyacrylamide gel electrophoresis (BN-PAGE). Curr. Protoc. Mouse Biol. 6, 1–14.

Kempen, J.H., O'Colmain, B.J., Leske, M.C., Haffner, S.M., Klein, R., Moss, S.E., Taylor, H.R., and Hamman, R.F.; Eye Diseases Prevalence Research Group (2004). The prevalence of diabetic retinopathy among adults in the United States. Arch. Ophthalmol. 122, 552–563.

Kim, H.J., Khalimonchuk, O., Smith, P.M., and Winge, D.R. (2012). Structure, function, and assembly of heme centers in mitochondrial respiratory complexes. Biochim. Biophys. Acta 1823, 1604–1616.

Kim, Y.M., Youn, S.W., Sudhahar, V., Das, A., Chandhri, R., Cuervo Grajal, H., Kweon, J., Leanhart, S., He, L., Toth, P.T., et al. (2018). Redox regulation of mitochondrial fission protein drp1 by protein disulfide isomerase limits endothelial senescence. Cell Rep. 23, 3565–3578.

Kizhakekuttu, T.J., Wang, J., Dharmashankar, K., Ying, R., Gutterman, D.D., Vita, J.A., and Widlansky, M.E. (2012). Adverse alterations in mitochondrial function contribute to type 2 diabetes mellitus-related endothelial dysfunction in humans. Arterioscler. Thromb. Vasc. Biol. 32, 2531–2539.

Kowluru, R.A., and Mishra, M. (2015). Oxidative stress, mitochondrial damage and diabetic

retinopathy. Biochim. Biophys. Acta 1852, 2474–2483.

Lee, I., Huttemann, M., Liu, J., Grossman, L.I., and Malek, M.H. (2012). Deletion of heart-type cytochrome c oxidase subunit 7a1 impairs skeletal muscle angiogenesis and oxidative phosphorylation. J. Physiol. 590, 5231–5243.

Lefevere, E., Toft-Kehler, A.K., Vohra, R., Kolko, M., Moons, L., and Van Hove, I. (2017). Mitochondrial dysfunction underlying outer retinal diseases. Mitochondrion 36, 66–76.

Lin, K.H., Xie, A., Rutter, J.C., Ahn, Y.R., Lloyd-Cowden, J.M., Nichols, A.G., Soderquist, R.S., Koves, T.R., Muoio, D.M., MacIver, N.J., et al. (2019). Systematic dissection of the metabolic-apoptotic interface in AML reveals heme biosynthesis to be a regulator of drug sensitivity. Cell Metab. 29, 1217–1231.

Lou, D.A., and Hu, F.N. (1987). Specific antigen and organelle expression of a long-term rhesus endothelial cell line. In Vitro Cell Dev Biol. 23, 75–85.

Magness, S.T., Maeda, N., and Brenner, D.A. (2002). An exon 10 deletion in the mouse ferrochelatase gene has a dominant-negative effect and causes mild protoporphyria. Blood 100, 1470–1477.

Makino, A., Scott, B.T., and Dillmann, W.H. (2010). Mitochondrial fragmentation and superoxide anion production in coronary endothelial cells from a mouse model of type 1 diabetes. Diabetologia 53, 1783–1794.

Navarro, S., Del Hoyo, P., Campos, Y., Abitbol, M., Moran-Jimenez, M.J., Garcia-Bravo, M., Ochoa, P., Grau, M., Montagutelli, X., Frank, J., et al. (2005). Increased mitochondrial respiratory chain enzyme activities correlate with minor extent of liver damage in mice suffering from erythropoietic protoporphyria. Exp. Dermatol. 14, 26–33.

Nilsson, R., Schultz, I.J., Pierce, E.L., Soltis, K.A., Naranuntarat, A., Ward, D.M., Baughman, J.M., Paradkar, P.N., Kingsley, P.D., Culotta, V.C., et al. (2009). Discovery of genes essential for heme biosynthesis through large-scale gene expression analysis. Cell Metab. 10, 119–130.

Pangare, M., and Makino, A. (2012). Mitochondrial function in vascular endothelial cell in diabetes. J. Smooth Muscle Res. 48, 1–26.

Pearlstein, D.P., Ali, M.H., Mungai, P.T., Hynes, K.L., Gewertz, B.L., and Schumacker, P.T. (2002). Role of mitochondrial oxidant generation in endothelial cell responses to hypoxia. Arterioscler Thromb. Vasc. Biol. 22, 566–573.

Petrillo, S., Chiabrando, D., Genova, T., Fiorito, V., Ingoglia, G., Vinchi, F., Mussano, F., Carossa, S., Silengo, L., Altruda, F., et al. (2018). Heme accumulation in endothelial cells impairs angiogenesis by triggering paraptosis. Cell Death Differ. 25, 573–588.

Picard, M., White, K., and Turnbull, D.M. (2013). Mitochondrial morphology, topology, and membrane interactions in skeletal muscle: a quantitative three-dimensional electron microscopy study. J. Appl. Physiol. 114, 161–171.

Poulos, T.L. (2014). Heme enzyme structure and function. Chem. Rev. *114*, 3919–3962.

Pran Babu, S.P.S., White, D., and Corson, T.W. (2020). Ferrochelatase regulates retinal neovascularization. FASEB J. https://doi.org/10.1096/fj.202000964R.

Rafikov, R., Sun, X., Rafikova, O., Meadows, M.L., Desai, A.A., Khalpey, Z., Yuan, J.X., Fineman, J.R., and Black, S.M. (2015). Complex I dysfunction underlies the glycolytic switch in pulmonary hypertensive smooth muscle cells. Redox Biol. *6*, 278–286.

Rolland, S.G., Motori, E., Memar, N., Hench, J., Frank, S., Winklhofer, K.F., and Conradt, B. (2013). Impaired complex IV activity in response to loss of LRPPRC function can be compensated by mitochondrial hyperfusion. Proc. Natl. Acad. Sci. U S A *110*, E2967–E2976.

Sapieha, P., Sirinyan, M., Hamel, D., Zaniolo, K., Joyal, J.S., Cho, J.H., Honore, J.C., Kermorvant-Duchemin, E., Varma, D.R., Tremblay, S., et al. (2008). The succinate receptor GPR91 in neurons has a major role in retinal angiogenesis. Nat. Med. *14*, 1067–1076.

Sapieha, P., Joyal, J.S., Rivera, J.C., Kermorvant-Duchemin, E., Sennlaub, F., Hardy, P., Lachapelle, P., and Chemtob, S. (2010). Retinopathy of prematurity: understanding ischemic retinal vasculopathies at an extreme of life. J. Clin. Invest. *120*, 3022–3032.

Shi, Z., and Ferreira, G.C. (2006). Modulation of inhibition of ferrochelatase by *N*-methylprotoporphyrin. Biochem. J. *399*, 21–28.

Sinkler, C.A., Kalpage, H., Shay, J., Lee, I., Malek, M.H., Grossman, L.I., and Huttemann, M. (2017). Tissue- and condition-specific isoforms of mammalian cytochrome c oxidase subunits: from function to human disease. Oxid Med. Cell Longev. *2017*, 1534056.

Sohoni, S., Ghosh, P., Wang, T., Kalainayakan, S.P., Vidal, C., Dey, S., Konduri, P.C., and Zhang, L. (2019). Elevated heme synthesis and uptake underpin intensified oxidative metabolism and tumorigenic functions in non-small cell lung cancer cells. Cancer Res. *79*, 2511–2525.

Tang, X., Luo, Y.X., Chen, H.Z., and Liu, D.P. (2014). Mitochondria, endothelial cell function, and vascular diseases. Front. Physiol. *5*, 175.

Vandekeere, S., Dewerchin, M., and Carmeliet, P. (2015). Angiogenesis revisited: an overlooked role of endothelial cell metabolism in vessel sprouting. Microcirculation *22*, 509–517.

Vandekeere, S., Dubois, C., Kalucka, J., Sullivan, M.R., Garcia-Caballero, M., Goveia, J., Chen, R., Diehl, F.F., Bar-Lev, L., Souffreau, J., et al. (2018). Serine synthesis via PHGDH is essential for heme production in endothelial cells. Cell Metab. *28*, 573–587.e13.

Vijayasarathy, C., Damle, S., Lenka, N., and Avadhani, N.G. (1999). Tissue variant effects of heme inhibitors on the mouse cytochrome c oxidase gene expression and catalytic activity of the enzyme complex. Eur. J. Biochem. *266*, 191–200.

Wang, Z., Zhao, H., Guan, W., Kang, X., Tai, X., and Shen, Y. (2018). Metabolic memory in mitochondrial oxidative damage triggers diabetic retinopathy. BMC Ophthalmol. *18*, 258.

Warren, C.M., Ziyad, S., Briot, A., Der, A., and Iruela-Arispe, M.L. (2014). A ligand-independent VEGFR2 signaling pathway limits angiogenic responses in diabetes. Sci. Signal. *7*, ra1.

Wellen, K.E., and Thompson, C.B. (2010). Cellular metabolic stress: considering how cells respond to nutrient excess. Mol. Cell *40*, 323–332.

Wyld, L., Burn, J.L., Reed, M.W., and Brown, N.J. (1997). Factors affecting aminolaevulinic acid-induced generation of protoporphyrin IX. Br. J. Cancer *76*, 705–712.

Zielinski, L.P., Smith, A.C., Smith, A.G., and Robinson, A.J. (2016). Metabolic flexibility of mitochondrial respiratory chain disorders predicted by computer modelling. Mitochondrion *31*, 45–55.

Supplemental Information

Heme Synthesis Inhibition Blocks Angiogenesis

via Mitochondrial Dysfunction

Trupti Shetty, Kamakshi Sishtla, Bomina Park, Matthew J. Repass, and Timothy W. Corson

Supplemental Figures
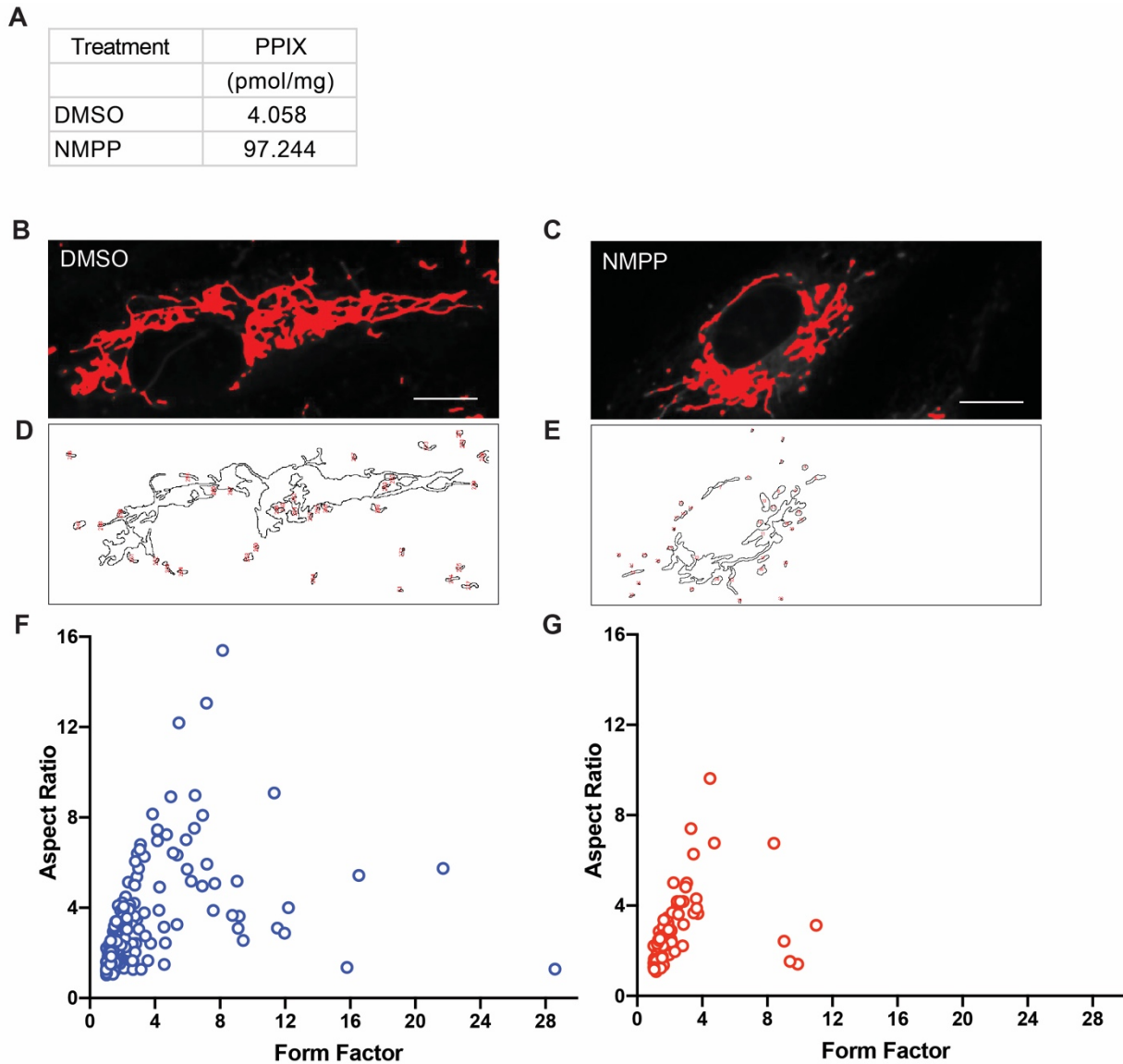
Figure S1. Mitochondrial morphometric analysis and PPIX levels in HRECs treated with NMPP, Related to Figure 1.
(A) PPIX levels quantified by ultra-performance liquid chromatography in HRECs treated with NMPP. Representative cells depicting particle analysis for measuring mitochondria. **(B, C)** Representative slice from Z-stack images showing threshold intensity set for DMSO and NMPP treated HRECs. **(D, E)** Representative slice from Z-stack images showing outlines of assessed mitochondria. **(F, G)** Correlation of form factor versus aspect ratio under DMSO and NMPP treatments for the representative cells shown above. Scale bars = 10 μm.
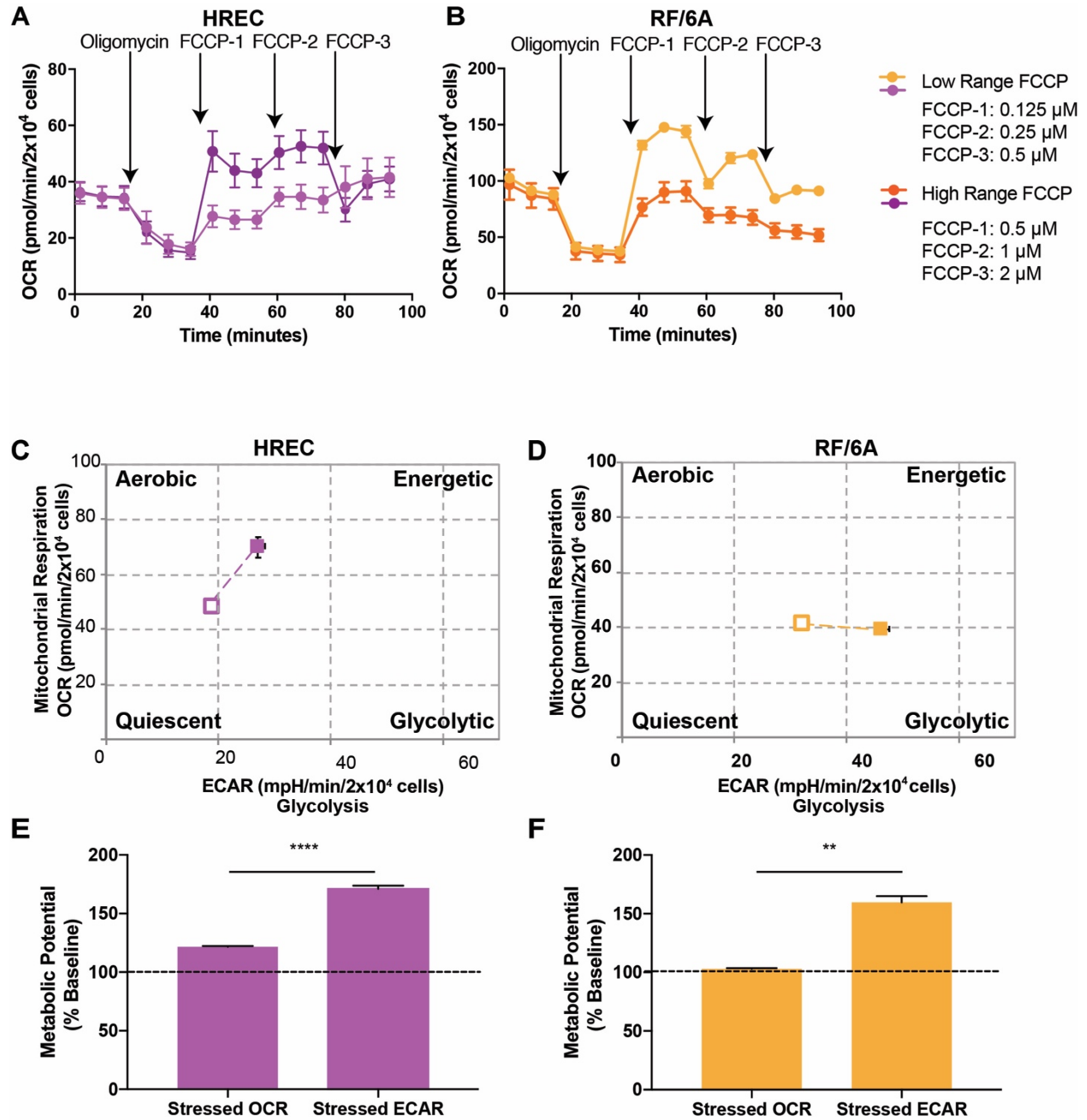
Figure S2. FCCP titration and cell energy phenotype of HRECs and RF/6A cells, Related to Transparent Methods and Figure 4.

Optimization of uncoupler FCCP concentration that produces maximal respiration in ocular endothelial cells. Oxygen consumption rate (OCR) traces of (**A**) HRECs and (**B**) RF/6A cells. 2×10^4 cells seeded. Mean ± SEM, n=3. Cellular energetic phenotype profiles under metabolic stress of (**C**) HRECs and (**D**) RF/6A cells. Open box indicates baseline phenotype, filled box indicates stressed phenotype. Representative plots of three independent experiments. Some error bars are too small to be seen. (**E, F**) % stressed OCR and ECAR produced over 100% baseline OCR and ECAR. Mean ± SEM, n=3; **p<0.01, ****p<0.0001, two-tailed unpaired Student's t-test.
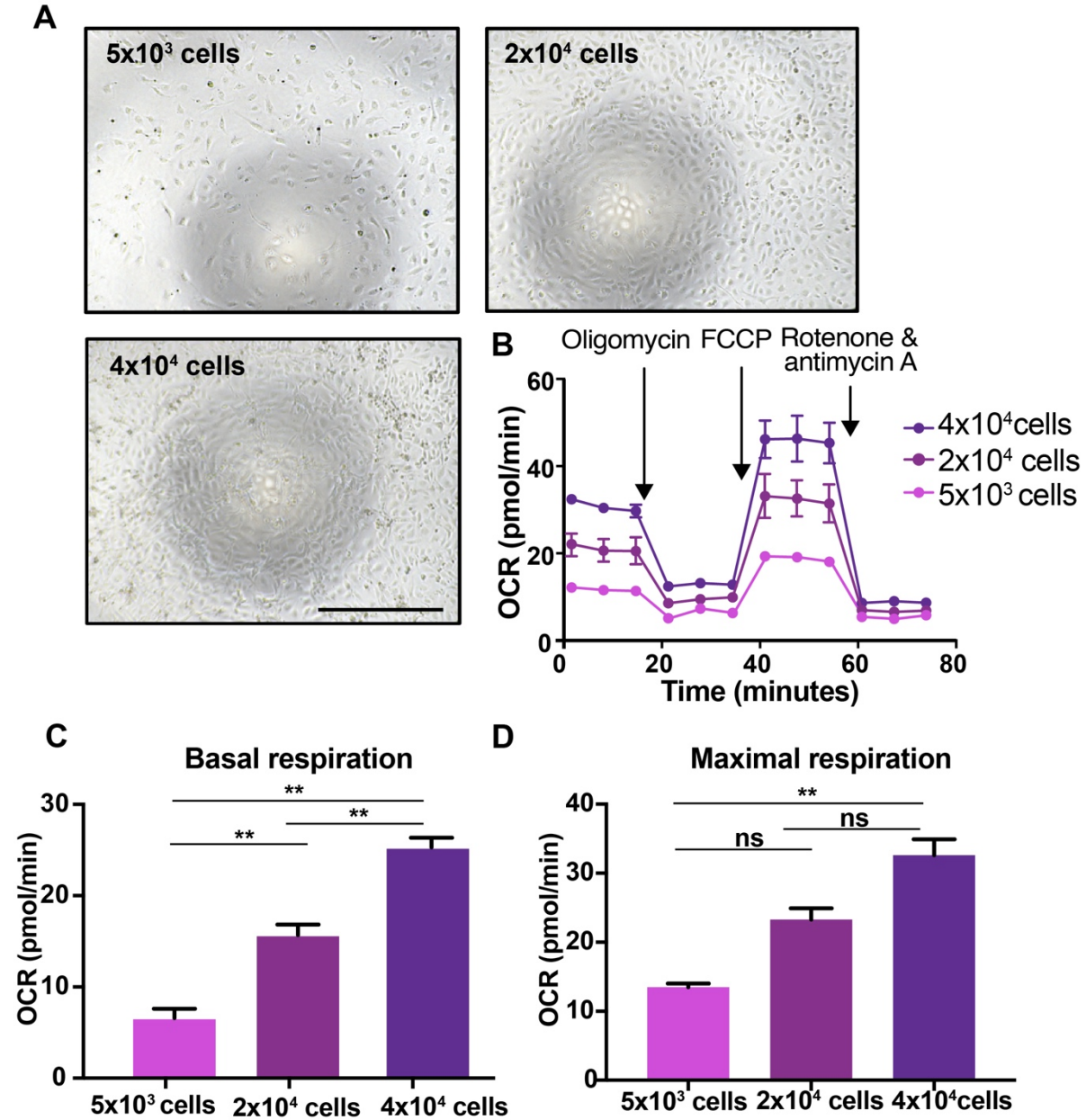
Figure S3. Optimizing cell seeding density, Related to Transparent Methods and Figure 4.
(A) Representative images from three independent experiments of HRECs. Scale bar = 500 μm. (B) Related OCR traces, (C) basal respiration, and (D) maximal respiration. Mean ± SEM, n=3; ns, not significant, **p<0.01, ANOVA with Tukey's post-hoc tests.
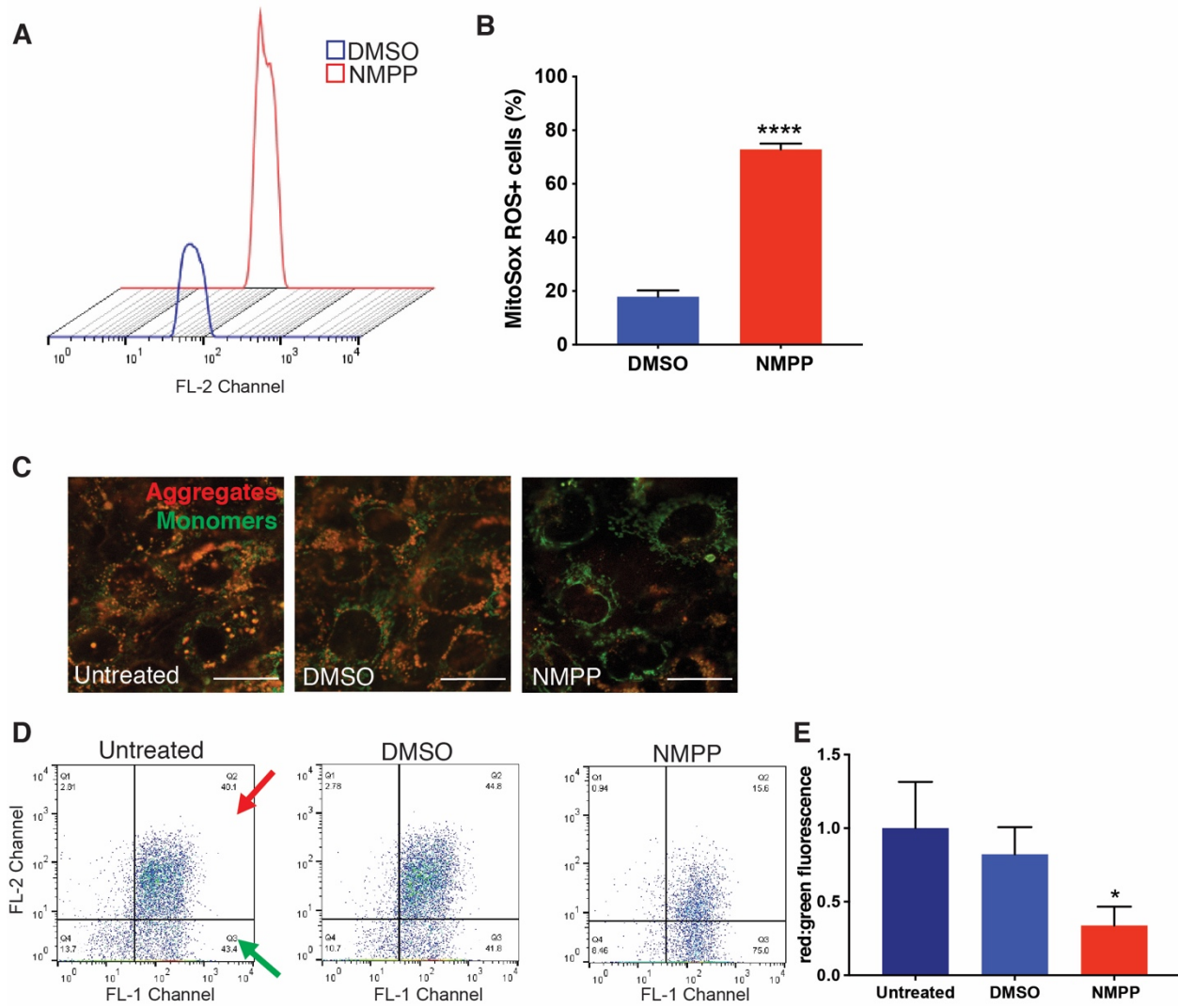
Figure S4. FECH blockade caused mitochondrial defects in RF/6A cells, Related to Figures 1 and 2. **(A)** RF/6A cells labeled with mitoSox ROS were assessed using flow cytometry. Representative fluorescence peaks. **(B)** Quantification of cells positive for red fluorescence. ****$p<0.0001$ vs. DMSO, unpaired Student's t-test**. (C)** RF/6A cells stained with JC-1 dye showing green monomers and red aggregates under NMPP treatment. **(D)** Representative dot plots of FL1 versus FL2 channel measuring red and green fluorescence using flow cytometry after NMPP treatment. Red and green arrows indicate quadrants expressing FL1-red and FL2-green fluorescent cells. **(E)** Quantification of red:green fluorescence from flow experiment. *$p<0.05$ vs. untreated, one-way ANOVA with Tukey's post hoc tests. Bar graphs indicate mean ± SEM, n=3; Scale bars = 20 μm.
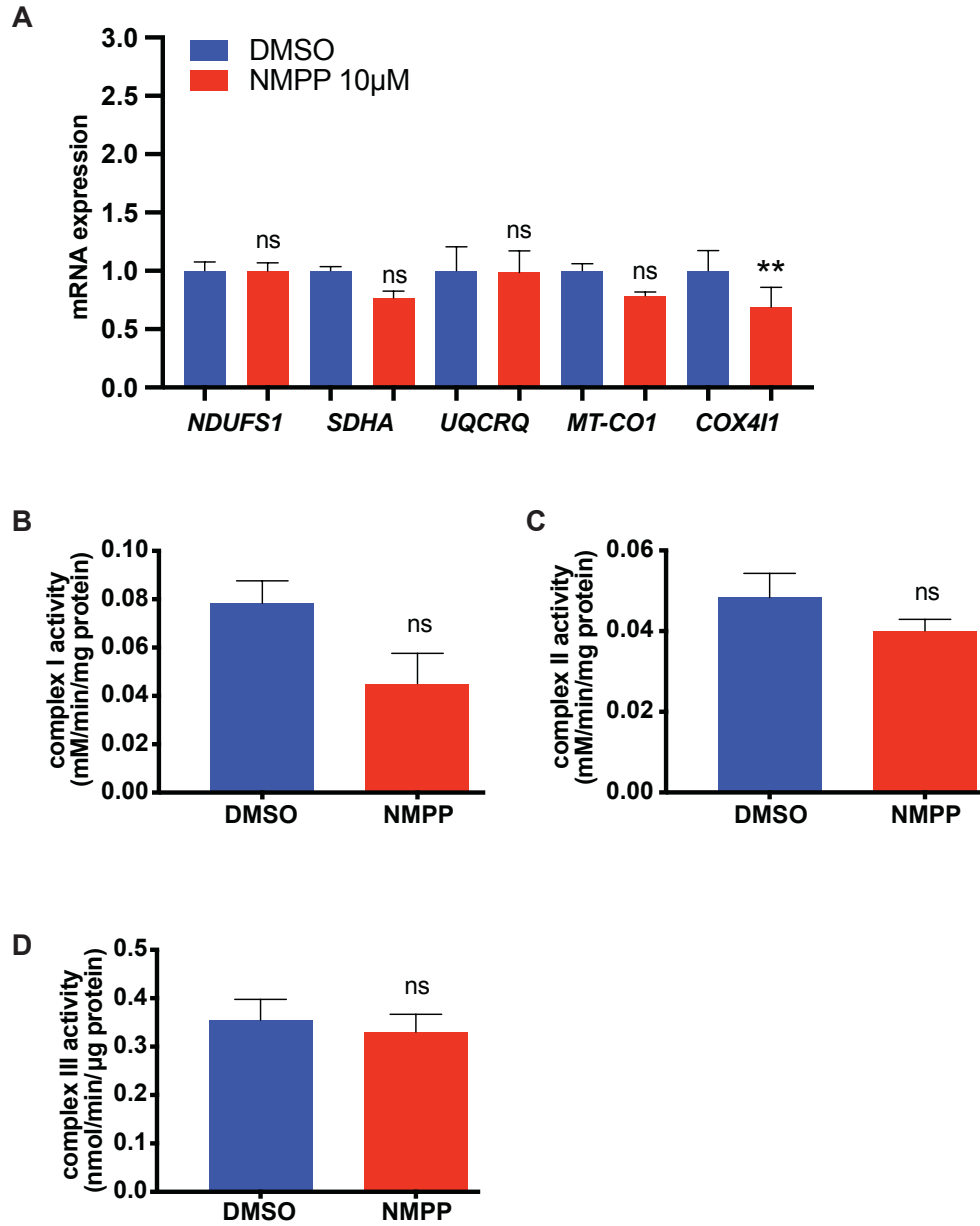
Figure S5. Loss of heme decreases transcription of nuclear encoded CcO but has no effect on activities of complexes I-III, Related to Figure 3.
(A) mRNA quantification of genes encoding components of ETC complexes I-IV (B-D) HRECs treated with NMPP were assessed for activities of (B) complex I, (C) complex II and (D) complex III. Bar graphs indicate mean ± SEM, n=3, ns = not significant, **p<0.01, unpaired Student's t-test.
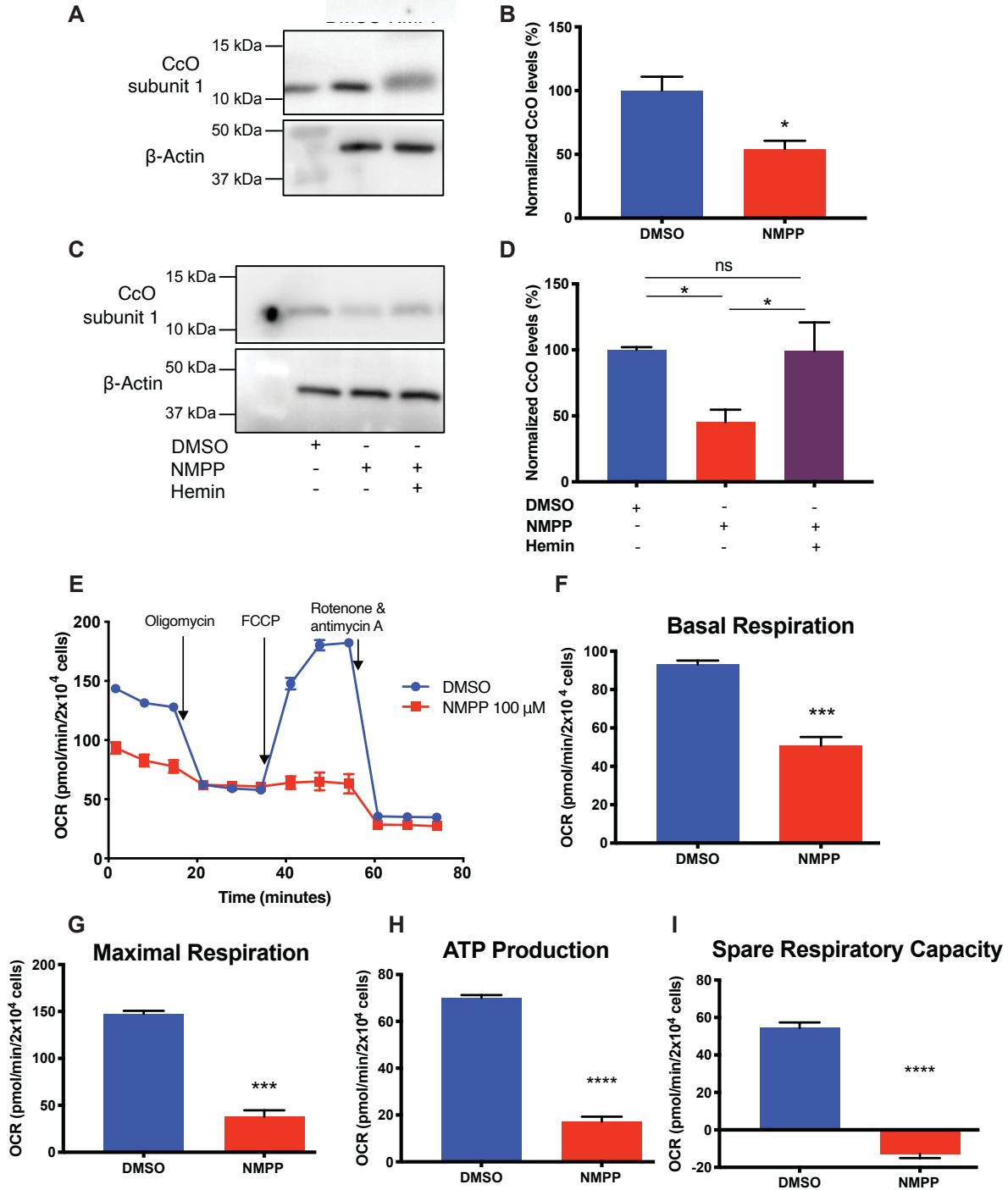
Figure S6. FECH inhibition decreases mitochondrial respiration and CcO expression, which is rescued by hemin in RF/6A cells, Related to Figures 3 and 4.
(A) RF/6A cells treated with NMPP were blotted for nuclear-encoded CcO subunit 1 (COX4I1) with **(B)** quantification as shown. **(C, D)** RF/6A cells treated with 100 μM NMPP show rescue of CcO subunit 1 protein levels after hemin supplementation. **(E)** Representative OCR kinetic traces for RF/6As under NMPP chemical inhibition. **(F)** Basal respiration, **(G)** maximal respiration, **(H)** OCR-linked ATP production, and **(I)** spare respiratory capacity were calculated based on OCR curves for the respective treatment group. Bar graphs indicate mean ± SEM, n=3; *p<0.05, ***p<0.001, ****p<0.0001, **(D)** one-way ANOVA with Tukey's post hoc tests; (**B, F-I**) unpaired Student's t-test.
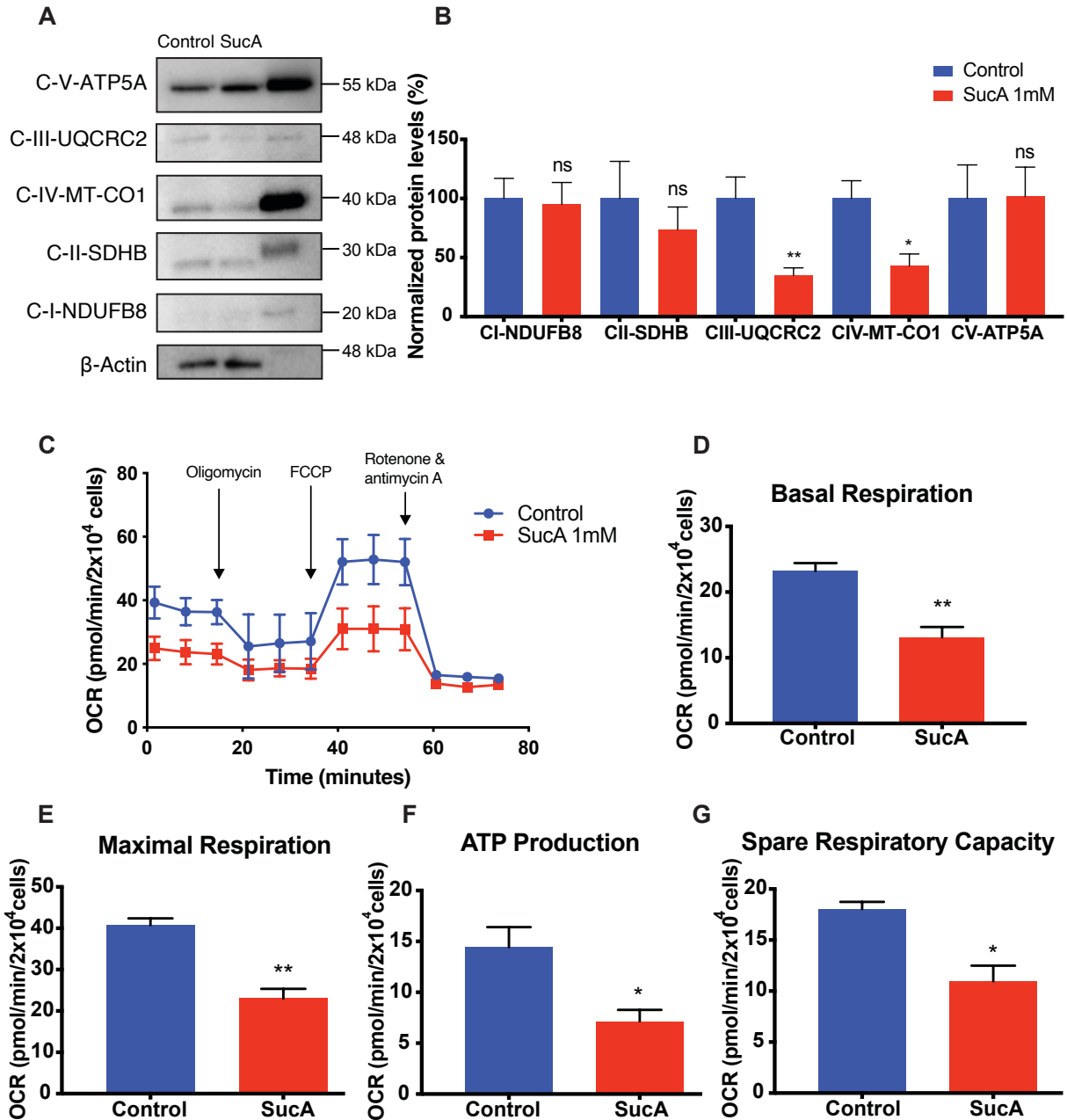
Figure S7. Loss of heme through ALAD blockade reduces mitochondrial respiration, Related to Figures 3 and 4.
(A) HRECs treated with succinylacetone were immunoblotted for Complexes I-V as indicated. **(B)** Quantification of the blots was graphed as shown relative to control. **(C)** OCR kinetic traces for HRECs under succinylacetone treatment. **(D)** Basal respiration, **(E)** maximal respiration, **(F)** OCR-linked ATP production, and **(G)** spare respiratory capacity were calculated based on OCR curves for the respective treatment group. Representative OCR curve of three individual experiments. Bar graphs indicate mean ± SEM, n=3; *p<0.05, **p<0.01, unpaired Student's t-test.

Transparent Methods

Experimental Model and Subject Details
Cell Culture
Human primary retinal microvascular endothelial cells (HRECs) and Attachment Factor were purchased from Cell Systems (Kirkland, WA, USA). Female HRECs were grown in endothelial growth medium (EGM-2) and used between passages 4 and 8. EGM-2 was prepared by combining components of an EGM-2 "bullet kit" (Cat no. CC-4176) and endothelial basal medium (EBM, Lonza, Walkersville, MD, USA; Cat No. CC-3156). As primary cells, these were not subject to authentication. Rhesus macaque choroidal endothelial (RF/6A) cells were obtained from ATCC (Manassas, VA, USA) and grown in Eagle's Minimum Essential Medium (EMEM, ATCC Cat No. 30-2003) supplemented with 10% fetal bovine serum (FBS, PAA Laboratories, Etobicoke, ON, Canada; Cat No. A15-751). Since short tandem repeat profiles are not available for Rhesus, these cells were not authenticated after receipt from the supplier, and sex was not reported. All cells were grown at 37°C, 5% CO_2, 100% humidity and tested for mycoplasma contamination regularly. *N*-methyl protoporphyrin (NMPP) was purchased from Frontier Scientific (Logan, Utah, USA), prepared in DMSO, and applied to cells at 1 μM or 10 μM (as indicated) for 48 hours. FECH siRNA (SASI_Hs01_00052189 and SASI_Hs01_00052190) was purchased from Sigma and MISSION® siRNA Universal from Sigma was used as a negative siRNA control. Succinylacetone (Sigma-Aldrich, Saint Louis, MO, USA) was prepared in sterile water and used at 1 mM final well concentration for 24 hours and water was used as vehicle control.

Animals
Animal studies were approved by the Indiana University School of Medicine Institutional Animal Care and Use Committee, and were consistent with the Association for Research in Vision and Ophthalmology Statement for the Use of Animals in Ophthalmic and Visual Research. C57BL/6J wild-type, healthy female mice, 8 weeks of age were purchased from Jackson Laboratories and group housed under standard conditions. NMPP at 10 μM final vitreous concentration was injected intravitreally into naïve mice under ketamine/xylazine anesthesia as described (Sulaiman et al., 2016), and 24 hrs post-injection, animals were euthanized, and retinas were immediately isolated from the animals and processed for the energetics experiment.

Method Details
Protoporphyrin IX quantification
Protoporphyrin IX (PPIX) analysis was performed at the Iron and Heme Core facility at the University of Utah. Cells were washed with PBS, pelleted, and stored frozen at -80°C. The cells were suspended in 50 mM potassium phosphate pH 7.4 and homogenized by sonication. 200 μL extraction solvent (EtOAc:HOAc, 4:1) was slowly added to 50 μL concentration-adjusted sample and shaken. The mixture was centrifuged at 16000x*g* for 0.5 min and the supernatant was collected. About 10 μL of the supernatant solution above was injected into a Waters Acquity ultra performance liquid chromatography (UPLC) system with an Acquity UPLC BEH C18, 1.7 μm, 2.1 x 100 mm column. PPIX was detected at 404 nm excitation and 630 nm emission. Solvent A was 0.2% aqueous formic acid while Solvent B was 0.2% formic acid in methanol. The flow rate was kept at 0.40 mL per minute and the column maintained at 60°C for the total run time of 7 min. The following successive linear gradient settings for run time in minutes versus Solvent A were as follows: 0.0, 80%; 2.5, 1%; 4.5, 1%; 5.0, 80%.

Mitochondrial morphology
Cells were plated on 35 mm coverslip bottom dishes. HRECs were stained using MitoTracker Green (Thermo Fisher, Cat no M7514) at 200 nM for 10 minutes in the dark at 37°C. Imaging was performed immediately following staining using an LSM700 confocal microscope (Zeiss, Thornwood, NY, USA) under a 63× oil immersion lens and acquired *Z*-stacked images were analyzed using ImageJ software (Trudeau et al., 2010). Briefly, individual cells were selected and particle analysis was performed to determine form factor (perimeter^2/4π*area) and aspect ratio (length of major and minor axes). Mitochondria of 12 cells per condition were analyzed and the mean per cell was considered for further statistical tests.

Mitochondrial membrane potential assessment

Membrane potential ($\Delta\Psi_m$) was measured with 5,5′,6,6′-tetrachloro-1,1′,3,3′-tetraethylbenzimidazolcarbo cyanine iodide (JC-1) (Santa Cruz, Santa Cruz, CA, USA) dye (Perelman et al., 2012). Cells were stained with JC-1 dye at 5 µg/mL final concentration for 10 minutes in the dark at 37°C. Cells were washed with 1× HBSS and prepared for flow cytometry (FACSCalibur, BD Biosciences, San Jose, CA) in Fluorobrite DMEM. JC-1 dye after accumulation in mitochondria forms red aggregates and green monomers that emit fluorescence at 590 nm and 510 nm respectively. For live imaging, cells grown in coverslip bottom 35mm dishes were stained and imaged using the Zeiss confocal microscope under a 63× oil immersion objective.

Mitochondrial ROS measurement

Cells were labeled with MitoSox ROS (Thermo Fisher Scientific) dye at 5 µM final concentration for 10 minutes in the dark at 37°C using phenol red-free Fluorobrite DMEM. Cells were washed and stained with Hoechst 33342 stain for 10 minutes at room temperature. For flow cytometry, cells were labeled with dye at 1 µM final concentration, incubated in the dark at 37°C and immediately loaded for ROS fluorescence detection in the FL-2 channel using flow cytometry (Kauffman et al., 2016).

mRNA quantification using qPCR

RNA was isolated using Trizol reagent and 1 µg RNA was used for cDNA synthesis, made using iScript cDNA synthesis kit from Bio Rad (Cat no. 1708897, Hercules, CA, USA). TaqMan probes for *MFN2* (Hs00208382_m1)*, DNM1L* (Hs01552605_m1)*, OPA1* (Hs01047013_m1)*, FECH* (Hs01555261_m1), *NDUFS1* (Hs00192297_m1), *SDHA* (Hs00188166_m1), *UQCRQ* (Hs00429571_g1), *MT-CO1* (Hs02596864_g1), and *COX4I1* (Hs00971639_m1) were purchased from Thermo Fisher Scientific (Pittsburgh, PA, USA). qPCR was performed using Fast Advanced Master Mix, TaqMan probes, and a ViiA7 thermal cycler (Applied Biosystems). Gene expression was determined using $\Delta\Delta C_t$ method and *HPRT* (Hs02800695_m1) as housekeeping control and normalized to individual sample controls.

Immunoblotting

Cells were lysed in RIPA buffer (Sigma-Aldrich, St. Louis, MO, USA, Cat no. R0278) and processed for protein quantification followed by SDS-PAGE. For ETC proteins, total OXPHOS Rodent WB Antibody Cocktail (Abcam, ab110413, Cambridge, MA, USA) at 1:250 dilution was used. CcO nuclear-encoded subunit 1 (COX4I1) antibody was purchased from Thermo Fisher Scientific (Cat no. PA5-19471, Pittsburgh, PA, USA) and used at 1:1000 dilution. β-actin antibody was purchased from Sigma (Cat no. A5441) and used at 1:2000 dilution. FECH antibody was purchased from LifeSpan BioSciences (Seattle, WA, USA, Cat no LS C409953) and used at 1:500 dilution prepared in 5% BSA solution. Chemiluminescent reagent ECL Prime was purchased from GE Healthcare (Buckinghamshire, UK, Cat no. RPN2232).

Complexes I-IV activity assays

For complex I activity, HRECs treated with NMPP (10 µM) or DMSO were harvested and processed using a kit (Abcam, Cambridge, MA, USA, Cat no. ab109721) according to manufacturer's instructions. Briefly, 250 µg of protein lysates were loaded into plates pre-coated with immobilized complex I and the oxidation of NADH to NAD+ was measured as the increase in absorbance at 450 nm, read on a Synergy H1 plate reader (BioTek, Winooski, VT, USA). Complex II enzyme activity was measured using an assay kit (Abcam, Cambridge, MA, USA, Cat no. ab109908) following manufacturer's instructions. Cell lysates from HRECs treated with either DMSO or NMPP (10 µM) were processed and 250 µg protein was loaded into plates coated with anti-complex II antibody. The activity of complex II was determined by measuring the production of ubiquinol coupled to the dye 2,6- dichlorophenolindophenol as a reduction in absorbance at 600 nm. For complex III activity, cell lysates from NMPP (10 µM) or DMSO treated HRECs were processed using complex II + III enzyme assay kit (Abcam, Cambridge, MA, USA, Cat no. ab109905) according to manufacturer's instructions. Complex III activity was determined as a gain in absorbance from the reaction of oxidized cytochrome *c* to the reduced form at 550 nm. ELISA was performed on cell lysates treated using Complex IV ELISA kit (Abcam, Cambridge, MA, USA, Cat no. ab109909) following manufacturer's instructions. Briefly, 10 µg protein was loaded into plates coated with CcO antibody and oxidation of reduced cytochrome *c* by the immunocaptured CcO from the sample was measured, using

absorbance at 550 nm. Kinetic reads were obtained and slopes directly correlating to enzyme activity were determined. Total amount of CcO was also assessed on the same samples.

Hemin rescue
For hemin rescue experiments, hemin (Sigma-Aldrich, Cat no H9039) 10 µM (final well concentration) was freshly prepared in DMSO. Cells pretreated with NMPP were supplemented with hemin in EBM2 containing 0.2% FBS for 6 hrs, followed by harvesting and processing for immunoblotting or ELISA.

FCCP titration, cell density determination, and cell energy phenotype
For determining optimal FCCP concentration, two ranges of FCCP were used (Figure S2A, B). Low range concentrations of 0.125, 0.25 and 0.5 µM and high range concentrations of 0.5, 1 and 2 µM were used for titration. We found 1 µM and 0.125 µM suitable for HRECs and RF/6A cells respectively. Similarly, for identification of appropriate cell seeding density to determine OCR and ECAR, cells at $5{\times}10^3$, $2{\times}10^4$ and $4{\times}10^4$ cells per well were plated overnight, and photographed using an EVOS fl digital microscope, followed by Seahorse XF analyses described below.

For assessment of cellular energy phenotype, cells ($2{\times}10^4$ per well) were grown, as indicated, overnight followed by assessment of metabolic phenotype using the Seahorse XFp Cell Energy Phenotype test kit (Cat. No. 103275-100). Stressor mix was prepared by combining 1 µM oligomycin and 0.125 or 1 µM FCCP. Cells were incubated in base medium containing glutamine, sodium pyruvate and glucose for 1 hour in a room air incubator prior to measurements. Five cycles of readings were taken after the injection of stressor mix on the cells and kinetic traces indicating OCR and ECAR were produced in tandem.

Mitochondrial energetics
For measuring mitochondrial function, oxygen consumption rate (OCR) was measured using the Seahorse XFp Cell Mito Stress test kit (Cat No. 103010-100) (Figure S3) (Dranka et al., 2011) at the Indiana University School of Medicine Angio BioCore. Cells ($2{\times}10^4$ per well) treated with NMPP (10 µM) or succinyl acetone (1 mM) were seeded overnight in XFp miniplates. Sensor cartridges were hydrated overnight in XF calibrant in a room air incubator. Next day, XF Base assay medium was prepared by addition of 5.5 mM glucose and 0.61 mM sodium pyruvate. For HRECs, 3.2 mM L-glutamine was used, while for RF/6A cells 1.6 mM concentration was used as per their respective routine culture medium compositions. Unbuffered base medium was filter sterilized followed by pH adjustment to 7.4 using 0.2 N NaOH solution. Cells were rinsed with base medium twice to remove overnight culture medium and this was replaced with base assay medium. Cells were incubated for a minimum of 1 hour in a room air incubator before proceeding with the assay. Mitochondrial inhibitors at final well concentrations of 1 µM oligomycin, 0.125 µM (for RF/6A cells) or 1 µM FCCP (for HRECs) and 0.5 µM rotenone/antimycin A were prepared using freshly buffered base medium. Mitochondrial inhibitors were then loaded into the hydrated sensor cartridges. After incubating cells in a room air incubator, XFp miniplates and the sensor cartridges were loaded into the instrument and OCR readings were determined using the XFp analyzer. The assay program was set up to measure three cycles of oligomycin followed by FCCP and a final injection of rotenone/antimycin A injected at indicated times. OCR in response to serial injections of oligomycin, FCCP and rotenone/antimycin mixture were recorded real-time in a kinetic assay.

For retinal ex vivo OCR measurements, protocols were adapted as previously described (Joyal et al., 2016; Kooragayala et al., 2015). Briefly, eyes were enucleated and retina was isolated from the posterior cup. Retinal punches (1 mm diameter) were dissected from an area adjacent to optic nerve to minimize variability in retinal thickness. Retinal punches were incubated in Seahorse XF DMEM Medium pH 7.4 containing 5 mM HEPES supplemented with 12 mM glucose and 2 mM L-glutamine for 1 hour in a room air incubator at 37°C. For OCR measurement, 0.5 µM FCCP and 0.5 µM rotenone/antimycin A were injected and OCR readings were determined.

Glycolytic function
Glycolytic parameters were measured using the Seahorse XF Glycolysis Stress test kit (Cat No. 103020-100). Cells ($2{\times}10^4$ per well) were grown overnight followed by glucose starvation in assay medium containing sodium pyruvate and glutamine for 1 hour in a room air incubator. Compounds modulating

glycolysis were prepared using the same assay medium. Glucose at a final well concentration of 10 mM, oligomycin at 1μM and 2-deoxyglucose at 50 mM were loaded onto ports of the hydrated sensor cartridge followed by measurement of extracellular acidification rate (ECAR) using the XFp analyzer.

Quantification and Statistical Analysis
All Seahorse kinetic traces were analyzed using Wave 2.4 software (Agilent) and GraphPad Prism v. 8.0. FCS files for flow cytometry were analyzed using FlowJo v10. Comparisons between groups were performed with either unpaired, two-tailed Student's t-test or one-way ANOVA with Tukey's post-hoc tests as indicated. p values < 0.05 were considered statistically significant. Mean±SEM shown for all graphs unless indicated otherwise; n is listed in figure legends.

Supplemental References

Joyal, J.S., Sun, Y., Gantner, M.L., Shao, Z., Evans, L.P., Saba, N., Fredrick, T., Burnim, S., Kim, J.S., Patel, G., et al. (2016). Retinal lipid and glucose metabolism dictates angiogenesis through the lipid sensor Ffar1. Nat Med 22, 439-445.

Kauffman, M.E., Kauffman, M.K., Traore, K., Zhu, H., Trush, M.A., Jia, Z., and Li, Y.R. (2016). MitoSOX-Based flow cytometry for detecting mitochondrial ROS. React Oxyg Species (Apex) 2, 361-370.

Kooragayala, K., Gotoh, N., Cogliati, T., Nellissery, J., Kaden, T.R., French, S., Balaban, R., Li, W., Covian, R., and Swaroop, A. (2015). Quantification of oxygen consumption in retina ex vivo demonstrates limited reserve capacity of photoreceptor mitochondria. Invest Ophthalmol Vis Sci 56, 8428-8436.

Perelman, A., Wachtel, C., Cohen, M., Haupt, S., Shapiro, H., and Tzur, A. (2012). JC-1: Alternative excitation wavelengths facilitate mitochondrial membrane potential cytometry. Cell Death Dis 3, e430.

Sulaiman, R.S., Merrigan, S., Quigley, J., Qi, X., Lee, B., Boulton, M.E., Kennedy, B., Seo, S.Y., and Corson, T.W. (2016). A novel small molecule ameliorates ocular neovascularisation and synergises with anti-VEGF therapy. Sci Rep 6, 25509.

Trudeau, K., Molina, A.J., Guo, W., and Roy, S. (2010). High glucose disrupts mitochondrial morphology in retinal endothelial cells: Implications for diabetic retinopathy. Am J Pathol 177, 447-455.